

## Accepted Manuscript

Vibration of tapered composite driveshaft based on the hierarchical finite element analysis

Majed Almuslmani, Rajamohan Ganesan

PII: S0263-8223(18)31661-1

DOI: <https://doi.org/10.1016/j.compstruct.2018.10.053>

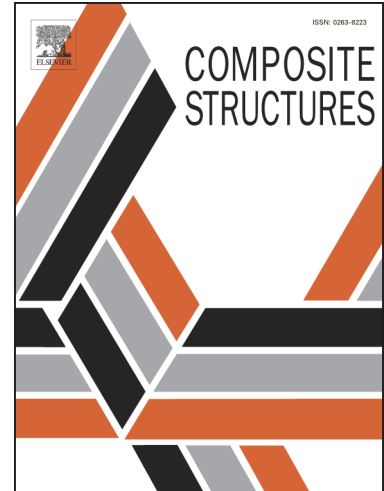
Reference: COST 10304

To appear in: *Composite Structures*

Received Date: 13 June 2018

Revised Date: 13 September 2018

Accepted Date: 18 October 2018



Please cite this article as: Almuslmani, M., Ganesan, R., Vibration of tapered composite driveshaft based on the hierarchical finite element analysis, *Composite Structures* (2018), doi: <https://doi.org/10.1016/j.compstruct.2018.10.053>

This is a PDF file of an unedited manuscript that has been accepted for publication. As a service to our customers we are providing this early version of the manuscript. The manuscript will undergo copyediting, typesetting, and review of the resulting proof before it is published in its final form. Please note that during the production process errors may be discovered which could affect the content, and all legal disclaimers that apply to the journal pertain.

**Revised Manuscript Draft**

**Title:** Vibration of tapered composite driveshaft based on the hierarchical finite element analysis

**Article Type:** Full Length Article

**Keywords:** Tapered composite shaft, Rotordynamics, Finite element method

**Corresponding Author:** Rajamohan Ganesan

**Corresponding Author's Institution:** Department of Mechanical, Industrial and Aerospace Engineering, Concordia University, Canada.

**Authors:** Majed Almuslmani and Rajamohan Ganesan

**Abstract:** In the aerospace and automotive applications driveshafts are manufactured using fiber reinforced composite materials. Compared to a conventional metallic driveshaft, a composite driveshaft gives higher natural frequencies and critical speeds, and lower vibration. They are also lightweight structures, especially when they are tapered. The design of the driveshaft is based on its fundamental natural frequency, and tapering the driveshaft can substantially improve the value of this natural frequency. In this study, the vibration analysis of the tapered composite driveshaft is carried out using the hierarchical finite element formulation, and for this purpose, the Timoshenko beam theory is used. In addition, the effects of rotary inertia, transverse shear deformation, gyroscopic force, axial load, coupling due to the lamination of composite layers, and taper angle are incorporated in the hierarchical finite element model. The potential energy and the kinetic energy of the tapered composite shaft are obtained, and then the equations of motion are developed using Lagrange's equation. The finite element solution is validated using the approximate solution based on the Rayleigh-Ritz method. A comprehensive parametric study is conducted based on the hierarchical finite element formulation.

# Vibration of tapered composite driveshaft based on the hierarchical finite element analysis

Majed. Almuslmani<sup>1</sup>, Rajamohan Ganesan<sup>2\*</sup>

<sup>1</sup> Department of Mechanical, Industrial and Aerospace Engineering, Concordia University, Canada

<sup>2</sup> Department of Mechanical, Industrial and Aerospace Engineering, Concordia University, Canada

\* Corresponding author (ganesan@encs.concordia.ca)

**Keywords:** (Tapered composite shaft, Rotordynamics, Finite element method)

## Abstract

In the aerospace and automotive applications driveshafts are manufactured using fiber reinforced composite materials. Compared to a conventional metallic driveshaft, a composite driveshaft gives higher natural frequencies and critical speeds, and lower vibration. They are also lightweight structures, especially when they are tapered. The design of the driveshaft is based on its fundamental natural frequency, and tapering the driveshaft can substantially improve the value of this natural frequency. In this study, the vibration analysis of the tapered composite driveshaft is carried out using the hierarchical finite element formulation, and for this purpose, the Timoshenko beam theory is used. In addition, the effects of rotary inertia, transverse shear deformation, gyroscopic force, axial load, coupling due to the lamination of composite layers, and taper angle are incorporated in the hierarchical finite element model. The potential energy and the kinetic energy of the tapered composite shaft are obtained, and then the equations of motion are developed using Lagrange's equation. The finite element solution is validated using

the approximate solution based on the Rayleigh-Ritz method. A comprehensive parametric study is conducted based on the hierarchical finite element formulation.

### NOMENCLATURE

$v$	Displacement of the shaft in y direction
$w$	Displacement of the shaft in z direction
$\beta_y$	Rotation of the shaft around y direction
$\beta_z$	Rotation of the shaft around z direction
$\Omega$	Rotational speed of the shaft
$\eta$	Fiber orientation angle
$\alpha$	Taper angle
$x, \theta, r$	Cylindrical coordinate system
$x, y, z$	Cartesian coordinate system
$U_{comp}$	Total strain energy of the composite shaft element
$U_{BS}$	Strain energy of the composite shaft that results from the bending moment and the shear force
$U_F$	External work done on the shaft due to a constant axial force
$T_{comp}$	Kinetic energy of the composite shaft element
[G]	Gyroscopic matrix
[M]	Mass matrix
[K]	Stiffness matrix

$[K_P]$	Geometric stiffness matrix due to axial load
$\dot{v}$	Translational velocity in y-direction
$\dot{w}$	Translational velocity in z-direction
$\dot{\beta}_y$	Angular velocity about the y-axis
$\dot{\beta}_z$	Angular velocity about the z-axis
$k_s$	Shear correction factor
$m_c$	Mass per unit length
$I_{dc}$	Diametral mass moment of inertia
$I_{pc}$	Polar mass moment of inertia
$L$	Length of the tapered composite element
$x$	Local axial coordinate of the element

## 1 Introduction

Composite materials are widely being used in aircraft and automobile structures, because they have high strength-and stiffness-to-mass ratio, good damping capacity, and high resistance to fatigue and corrosion. These characteristics have attracted the manufacturers in aerospace and automobile industries, and currently there is a desire to replace the conventional metal driveshaft by the shaft that is manufactured using composite materials. It is required of the driveshaft to avoid the resonance phenomena during the operation, and this can be achieved by designing the composite driveshaft with high bending natural frequency and high first critical speed. In the case of the conventional metal driveshaft, it has been found that tapering the driveshaft, in a way that the inner and outer diameters of one end is constant and the inner and outer diameters of the other end increase with the taper angle, improves the natural frequency and first critical speed. Such a tapering can be achieved in the composite driveshaft using filament winding machine and fiber placement machine.

Zinberg and Symonds [1] experimentally obtained the natural frequency and critical speed of a boron/epoxy composite shaft, and they compared the results with other results that were obtained for an aluminum shaft. The comparison shows the advantages of the composite shaft over the aluminum shaft. Chang et al. [2] developed Lagrangian finite element model to perform rotordynamic analysis of uniform composite shaft, and the model was based on Timoshenko beam theory. Chang et al. [3] studied the vibrations of the rotating composite shafts containing randomly oriented reinforcements. Boukhalfa and Hadjoui [4] studied the free vibration of uniform composite shaft using the hierarchical finite element method. In addition, Almuslmani

and Ganesan [5] developed a finite element model using Hermitian – conventional finite element for rotordynamic analysis of uniform composite shaft. Qatu and Iqbal [6] developed an exact solution based on the Euler–Bernoulli beam theory to obtain the natural frequency of a two segmented composite driveshaft joined by a hinge; they showed the effect of considering the mass of the hinge on the natural frequency. In addition, Chen and Peng [7] used Timoshenko beam theory and finite element model to analyse the dynamic behavior of a composite shaft subjected to axial periodic forces and to determine the regions of dynamic instability. Librescu et al. [8] studied the stability of rotating tapered composite shaft subjected to an axial compressive force. The results showed that tapering the composite shaft shifts the domain of divergence and flutter instability to larger rotating speeds.

This paper utilizes hierarchical finite element method (HFEM) to perform rotodynamic analysis on tapered composite shaft. The method has been suggested in many papers [4] and [9 -12].

Using hierarchical finite element, simple structure such as the tapered composite shaft can be represented in one element and variable numbers of hierarchical terms, and the desired accuracy degree of result can be accomplished not only by increasing the element numbers as in conventional finite element method but also by increasing the number of hierarchical terms.

Comparing to conventional finite element, HFEM yields more accurate results for eigenvalue problems of the same order [11]. Moreover, the hierarchical terms can be represented either in trigonometric terms or Legendre orthogonal polynomials terms. Legendre orthogonal polynomials generally are used as hierarchical terms in HFEM, however, they limit the use of HFEM in high-frequency analysis because they lead to numerical rounding errors associated with floating point arithmetic that increase with increasing order of polynomial [11-12]. In this

paper, hierarchical terms are represented in trigonometric function while the polynomial shape function are used to describe the element's nodal degrees of freedom.

For developing a finite element model of tapered composite driveshaft for rotordynamic analysis, in the present work, the hierarchical finite element formulation with trigonometric shape functions is used. The new finite element model takes into account the effects of the axial load, the rotary inertia, the gyroscopic forces, the taper angle, and the coupling effects due to the lamination of composite layers. In addition, Timoshenko beam theory is adopted, so that the effect of shear deformation can be considered. After obtaining the equations of motion using Lagrange's equation, the present tapered composite shaft model is validated using Rayleigh-Ritz approximate solution for simply supported condition. A comprehensive parametric study is conducted to investigate the dynamic behavior of tapered composite driveshaft.

## 2 Energy expressions of the tapered composite shaft

The kinetic energy of the tapered composite shaft finite element, denoted by  $T_{comp}$ , can be written as

$$T_{comp} = \frac{1}{2} \int_0^L m_c(x) (\dot{v}^2 + \dot{w}^2) dx + \frac{1}{2} \int_0^L I_{dc}(x) (\dot{\beta}_y^2 + \dot{\beta}_z^2) dx - \int_0^L I_{pc}(x) \Omega \dot{\beta}_z \beta_y dx \quad (1)$$

where  $m_c$ ,  $I_{dc}$ ,  $I_{pc}$ ,  $\dot{v}$ ,  $\dot{w}$ ,  $\dot{\beta}_y$ ,  $\dot{\beta}_z$ ,  $L$ ,  $x$  and  $\Omega$  are the mass per unit length, diametral mass moment of inertia, the polar mass moment of inertia, the translational velocity in y-direction, the translational velocity in z-direction, the angular velocity about the y-axis, the angular velocities

about the z-axis, the length of the tapered composite element, the local axial coordinate of the element, and the rotational speed of the shaft respectively.  $m_c$ ,  $I_{dc}$ , and  $I_{pc}$  can be expressed as

$$m_c(x) = \pi \sum_{s=1}^n \rho_s (r_{os}^2(x) - r_{is}^2(x)) \quad (2)$$

$$I_{dc}(x) = \frac{\pi}{4} \sum_{s=1}^n \rho_s (r_{os}^4(x) - r_{is}^4(x)) \quad (3)$$

$$I_{pc}(x) = \frac{\pi}{2} \sum_{s=1}^n \rho_s (r_{os}^4(x) - r_{is}^4(x)) \quad (4)$$

where  $n$  is the number of the layers in the laminate, and  $\rho_s$  is the density of the layer, and  $r_{os}$  and  $r_{is}$  are the outer radius and inner radius along the length for each single layer of the tapered shaft element, respectively. For the linear taper, the outer radius and inner radius for each single layer of the tapered shaft element are

$$r_{os}(x) = \left(1 - \frac{x}{L}\right)r_{o1} + \frac{x}{L}r_{o2} \quad (5)$$

$$r_{is}(x) = \left(1 - \frac{x}{L}\right)r_{i1} + \frac{x}{L}r_{i2} \quad (6)$$

where  $r_{i1}$  and  $r_{o1}$  are the inner and outer radii of the smallest diameter of the tapered element while  $r_{i2}$  and  $r_{o2}$  are the inner and outer radii of largest diameter of the tapered element as illustrated in Figure 1. Figure 2 shows a single lamina deformed into a conical tube with a linear taper angle  $\alpha$ . The principal material directions are denoted by 1, 2, and 3. The axis 1' extends along the tapered tube surface while 3'-axis is perpendicular to the same surface. The fiber angle  $\eta$  is the angle between 1-axis and 1'-axis and the angle between 2-axis and 2'-axis. To obtain the strain energy of the tapered composite shaft, it is required to find the stress-strain

relations in cylindrical coordinate system  $(x, \theta, r)$ . These relations can be obtained by considering the stress-strain relations for a lamina in the principal material coordinates and then applying a sequence of transformations to take into account the fiber orientation angle and the taper angle. Performing this, the stress-strain relations in cylindrical coordinate system  $(x, \theta, r)$  are obtained as

$$[\sigma_{x\theta r}] = [\bar{Q}][\varepsilon_{x\theta r}] = [T_3][T_1][Q][T_2]^{-1}[T_4]^{-1}[\varepsilon_{x\theta r}] \quad (7)$$

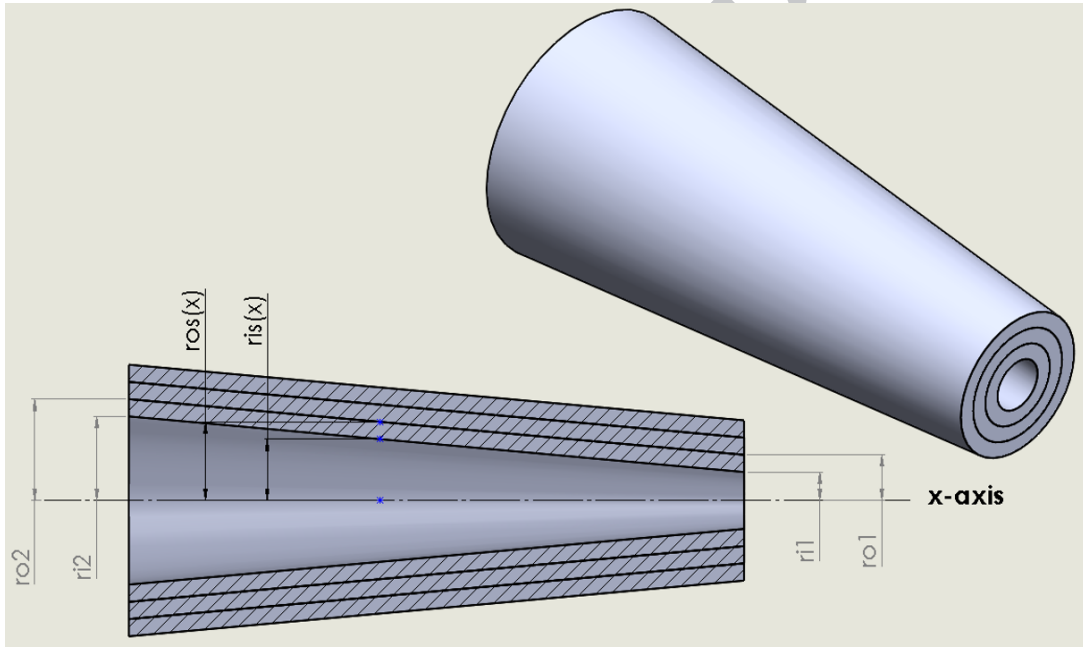


Fig.1. Tapered shaft element

where  $[Q]$  is the stiffness matrix of a single lamina.  $[\bar{Q}]$  is the transformed stiffness of the layer obtained after performing the rotation  $\eta$  about 3-axis in principal material coordinate system  $(1, 2, 3)$  and then performing the rotation  $\alpha$  about 2'-axis in primed coordinate system  $(1', 2', 3')$ .

$$[T_1] = \begin{bmatrix} m^2 & n^2 & 0 & 0 & 0 & 2mn \\ n^2 & m^2 & 0 & 0 & 0 & -2mn \\ 0 & 0 & 1 & 0 & 0 & 0 \\ 0 & 0 & 0 & m & -n & 0 \\ 0 & 0 & 0 & n & m & 0 \\ -mn & mn & 0 & 0 & 0 & m^2 - n^2 \end{bmatrix} \quad (8)$$

$$[T_2] = \begin{bmatrix} m^2 & n^2 & 0 & 0 & 0 & mn \\ n^2 & m^2 & 0 & 0 & 0 & -mn \\ 0 & 0 & 1 & 0 & 0 & 0 \\ 0 & 0 & 0 & m & -n & 0 \\ 0 & 0 & 0 & n & m & 0 \\ -2mn & 2mn & 0 & 0 & 0 & m^2 - n^2 \end{bmatrix} \quad (9)$$

$$[T_3] = \begin{bmatrix} c^2 & 0 & s^2 & 0 & 2sc & 0 \\ 0 & 1 & 0 & 0 & 0 & 0 \\ s^2 & 0 & c^2 & 0 & -2sc & 0 \\ 0 & 0 & 0 & c & 0 & -s \\ -sc & 0 & sc & 0 & c^2 - s^2 & 0 \\ 0 & 0 & 0 & s & 0 & c \end{bmatrix} \quad (10)$$

$$[T_4] = \begin{bmatrix} c^2 & 0 & s^2 & 0 & sc & 0 \\ 0 & 1 & 0 & 0 & 0 & 0 \\ s^2 & 0 & c^2 & 0 & -sc & 0 \\ 0 & 0 & 0 & c & 0 & -s \\ -2sc & 0 & 2sc & 0 & c^2 - s^2 & 0 \\ 0 & 0 & 0 & s & 0 & c \end{bmatrix} \quad (11)$$

$$m = \cos \eta; n = \sin \eta$$

$$c = \cos \alpha; s = \sin \alpha$$

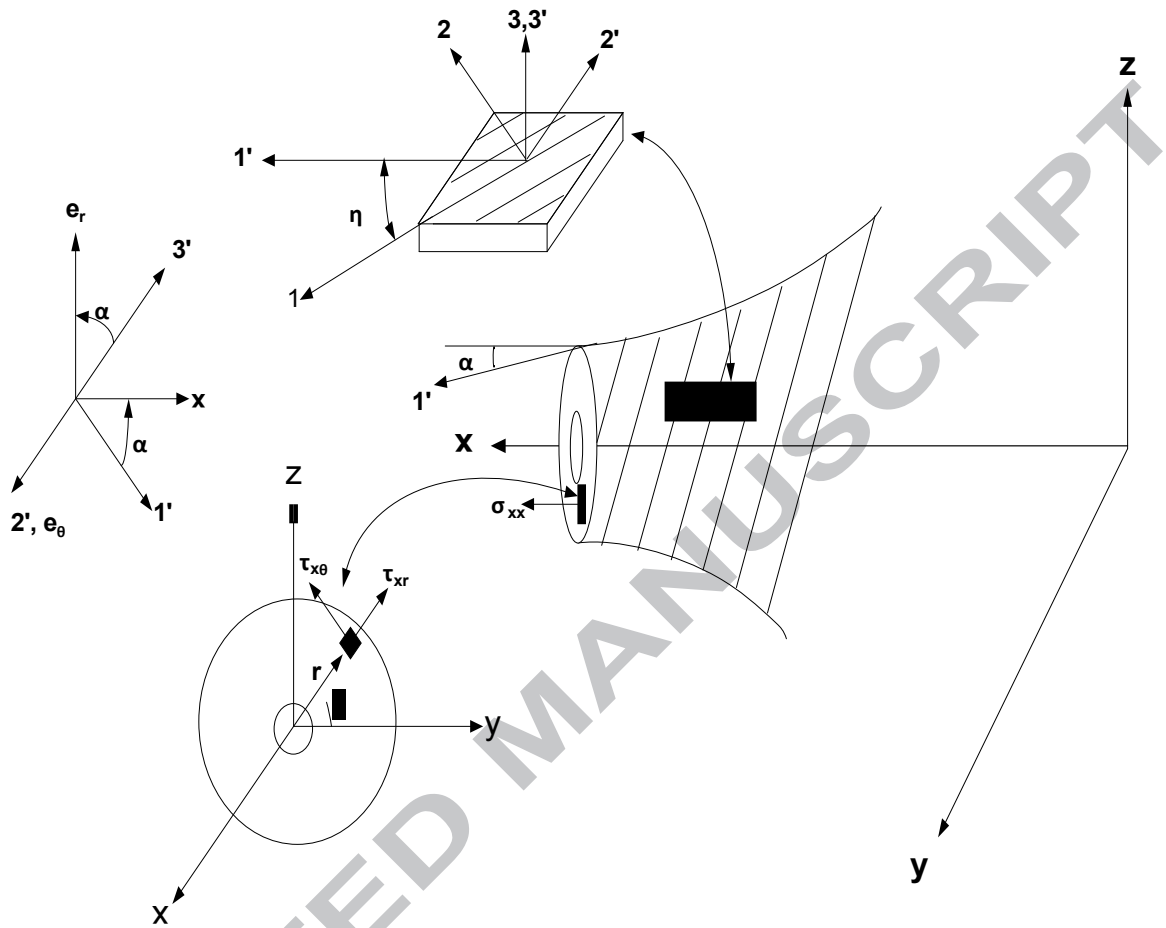


Fig. 2. Single composite lamina deformed into tapered cylinder

Based on Timoshenko beam theory, the displacement field of the cross-section of the tapered composite shaft can be described by the following equations:

$$u_x(x,y,z,t) = z\beta_y(x,t) - y\beta_z(x,t) = (r\sin\theta)\beta_y(x,t) - (r\cos\theta)\beta_z(x,t) \quad (12)$$

$$u_y(x,y,z,t) = v(x,t) \quad (13)$$

$$u_z(x,y,z,t) = w(x,t) \quad (14)$$

where  $y = r \cos \theta$  and  $z = r \sin \theta$ .  $u_x, u_y$  and  $u_z$  are the displacements of any point of the composite shaft in x, y and z directions, and  $v$  and  $w$  are the displacements of a point on the reference axis of the shaft in y and z directions and  $\beta_y$  and  $\beta_z$  are the rotation angles of the cross-section about y-axis and z-axis. Using Equations (12) - (14), the strains can be obtained as

$$\epsilon_{xx} = \frac{\partial u_x}{\partial x} = z \frac{\partial \beta_y}{\partial x} - y \frac{\partial \beta_z}{\partial x} \quad (15)$$

$$\epsilon_{yy} = \frac{\partial u_y}{\partial y} = 0 \quad (16)$$

$$\epsilon_{zz} = \frac{\partial u_z}{\partial z} = 0 \quad (17)$$

$$\gamma_{yz} = \frac{\partial u_z}{\partial y} + \frac{\partial u_y}{\partial z} = 0 \quad (18)$$

$$\gamma_{xz} = \frac{\partial u_x}{\partial z} + \frac{\partial u_z}{\partial x} = \beta_y + \frac{\partial w}{\partial x} \quad (19)$$

$$\gamma_{xy} = \frac{\partial u_x}{\partial y} + \frac{\partial u_y}{\partial x} = -\beta_z + \frac{\partial v}{\partial x} \quad (20)$$

The strain components in cylindrical coordinate system  $(x, \theta, r)$  can be written in terms of the strains in the Cartesian coordinate system  $(x, y, z)$  as

$$\begin{bmatrix} \epsilon_{xx} \\ \epsilon_{\theta\theta} \\ \epsilon_{rr} \\ \gamma_{\theta r} \\ \gamma_{xr} \\ \gamma_{x\theta} \end{bmatrix} = \begin{bmatrix} 1 & 0 & 0 & 0 & 0 & 0 \\ 0 & h^2 & g^2 & -2gh & 0 & 0 \\ 0 & g^2 & h^2 & 2gh & 0 & 0 \\ 0 & -gh & gh & g^2 - h^2 & 0 & 0 \\ 0 & 0 & 0 & 0 & h & g \\ 0 & 0 & 0 & 0 & g & -h \end{bmatrix} \begin{bmatrix} \epsilon_{xx} \\ \epsilon_{yy} \\ \epsilon_{zz} \\ \gamma_{yz} \\ \gamma_{xz} \\ \gamma_{xy} \end{bmatrix} \quad (21)$$

where  $g = \cos \theta$  and  $h = \sin \theta$ . Substituting Equations (15) – (20) into Equation (21), one can get

$$\epsilon_{xx} = r (\sin \theta) \frac{\partial \beta_y}{\partial x} - r (\cos \theta) \frac{\partial \beta_z}{\partial x} \quad (22)$$

$$\epsilon_{\theta\theta} = 0 \quad (23)$$

$$\epsilon_{rr} = 0 \quad (24)$$

$$\gamma_{\theta r} = 0 \quad (25)$$

$$\gamma_{xr} = (\sin \theta) \left( \frac{\partial w}{\partial x} + \beta_y \right) + (\cos \theta) \left( -\beta_z + \frac{\partial v}{\partial x} \right) \quad (26)$$

$$\gamma_{x\theta} = (\cos \theta) \left( \frac{\partial w}{\partial x} + \beta_y \right) - (\sin \theta) \left( -\beta_z + \frac{\partial v}{\partial x} \right) \quad (27)$$

By considering Equations (23) – (25) the stress – strain relations in Equation (7) can be written as

$$\begin{bmatrix} \sigma_{xx} \\ \sigma_{\theta\theta} \\ \sigma_{rr} \\ \tau_{\theta r} \\ \tau_{xr} \\ \tau_{x\theta} \end{bmatrix} = \begin{bmatrix} \bar{Q}_{11} & \bar{Q}_{15} & \bar{Q}_{16} \\ \bar{Q}_{21} & \bar{Q}_{25} & \bar{Q}_{26} \\ \bar{Q}_{31} & \bar{Q}_{35} & \bar{Q}_{36} \\ \bar{Q}_{41} & \bar{Q}_{45} & \bar{Q}_{46} \\ \bar{Q}_{51} & \bar{Q}_{55} & \bar{Q}_{56} \\ \bar{Q}_{61} & \bar{Q}_{65} & \bar{Q}_{66} \end{bmatrix} \begin{bmatrix} \epsilon_{xx} \\ \gamma_{xr} \\ \gamma_{x\theta} \end{bmatrix} \quad (28)$$

In Timoshenko beam theory, the shear correction factor  $k_s$  is used to adjust the stress state. By introducing the shear correction factor  $k_s$  in a way [2] that the stress – strain relations in Equation (28) can be modified to include the shear correction factor  $k_s$  and expressed as

$$\begin{bmatrix} \sigma_{xx} \\ \sigma_{\theta\theta} \\ \sigma_{rr} \\ \tau_{\theta r} \\ \tau_{xr} \\ \tau_{x\theta} \end{bmatrix} = \begin{bmatrix} \bar{Q}_{11} & k_s \bar{Q}_{15} & k_s \bar{Q}_{16} \\ \bar{Q}_{21} & k_s \bar{Q}_{25} & k_s \bar{Q}_{26} \\ \bar{Q}_{31} & k_s \bar{Q}_{35} & k_s \bar{Q}_{36} \\ k_s \bar{Q}_{41} & k_s \bar{Q}_{45} & k_s \bar{Q}_{46} \\ k_s \bar{Q}_{51} & k_s \bar{Q}_{55} & k_s \bar{Q}_{56} \\ k_s \bar{Q}_{61} & k_s \bar{Q}_{65} & k_s \bar{Q}_{66} \end{bmatrix} \begin{bmatrix} \varepsilon_{xx} \\ \gamma_{xr} \\ \gamma_{x\theta} \end{bmatrix} \quad (29)$$

The strain energy of tapered composite shaft due to bending moments and shear forces is

$$U_{BS} = \frac{1}{2} \iiint_V [\sigma_{x\theta r}]^T [\varepsilon_{x\theta r}] dV \quad (30)$$

Considering Equations (22) - (27) the strain energy  $U_{BS}$  can be written as

$$U_{BS} = \frac{1}{2} \int_0^L \left[ M_y \frac{\partial \beta_y}{\partial x} + M_z \frac{\partial \beta_z}{\partial x} + Q_y \left( \frac{\partial v}{\partial x} - \beta_z \right) + Q_z \left( \beta_y + \frac{\partial w}{\partial x} \right) \right] dx \quad (31)$$

where

$$M_y = \int_A \sigma_{xx} r \sin \theta dA \quad (32)$$

$$M_z = - \int_A \sigma_{xx} r \cos \theta dA \quad (33)$$

$$Q_{xr}^{(1)} = \int_A \tau_{xr} \sin \theta dA \quad (34)$$

$$Q_{xr}^{(2)} = \int_A \tau_{xr} \cos \theta dA \quad (35)$$

$$Q_{x\theta}^{(1)} = \int_A \tau_{x\theta} \sin \theta dA \quad (36)$$

$$Q_{x\theta}^{(2)} = \int_A \tau_{x\theta} \cos \theta \, dA \quad (37)$$

After applying the integrations in Equations (32) – (37), the stress resultants and stress couples of the tapered composite shaft are

$$M_y = \bar{D}_{11} \frac{\partial \beta_y}{\partial x} + \bar{B}_{15} k_s \left( \beta_y + \frac{\partial w}{\partial x} \right) + \frac{1}{2} \bar{B}_{16} k_s \left( \beta_z - \frac{\partial v}{\partial x} \right) \quad (38)$$

$$M_z = \bar{D}_{11} \frac{\partial \beta_z}{\partial x} - \bar{B}_{15} k_s \left( \frac{\partial v}{\partial x} - \beta_z \right) - \frac{1}{2} \bar{B}_{16} k_s \left( \beta_y + \frac{\partial w}{\partial x} \right) \quad (39)$$

$$Q_{xr}^{(1)} = \bar{B}_{51} k_s \frac{\partial \beta_y}{\partial x} + k_s \bar{A}_{55} \left( \beta_y + \frac{\partial w}{\partial x} \right) + k_s \bar{A}_{56} \left( \beta_z - \frac{\partial v}{\partial x} \right) \quad (40)$$

$$Q_{xr}^{(2)} = -\bar{B}_{51} k_s \frac{\partial \beta_z}{\partial x} + k_s \bar{A}_{55} \left( \frac{\partial v}{\partial x} - \beta_z \right) + k_s \bar{A}_{56} \left( \beta_y + \frac{\partial w}{\partial x} \right) \quad (41)$$

$$Q_{x\theta}^{(1)} = \frac{1}{2} \bar{B}_{61} k_s \frac{\partial \beta_y}{\partial x} + k_s \bar{A}_{65} \left( \beta_y + \frac{\partial w}{\partial x} \right) + k_s \bar{A}_{66} \left( \beta_z - \frac{\partial v}{\partial x} \right) \quad (42)$$

$$Q_{x\theta}^{(2)} = -\frac{1}{2} \bar{B}_{61} k_s \frac{\partial \beta_z}{\partial x} + k_s \bar{A}_{65} \left( \frac{\partial v}{\partial x} - \beta_z \right) + k_s \bar{A}_{66} \left( \beta_y + \frac{\partial w}{\partial x} \right) \quad (43)$$

where

$$\bar{A}_{66}(x) = \frac{\pi}{2} \sum_{s=1}^n \bar{Q}_{66} (r_{os}^2(x) - r_{is}^2(x)) \quad (44)$$

$$\bar{A}_{65}(x) = \frac{\pi}{2} \sum_{s=1}^n \bar{Q}_{65} (r_{os}^2(x) - r_{is}^2(x)) \quad (45)$$

$$\bar{A}_{55}(x) = \frac{\pi}{2} \sum_{s=1}^n \bar{Q}_{55} (r_{os}^2(x) - r_{is}^2(x)) \quad (46)$$

$$\bar{A}_{56}(x) = \frac{\pi}{2} \sum_{s=1}^n \bar{Q}_{56} (r_{os}^2(x) - r_{is}^2(x)) \quad (47)$$

$$\bar{B}_{16}(x) = \frac{2}{3}\pi \sum_{s=1}^n \bar{Q}_{16}(r_{os}^3(x) - r_{is}^3(x)) \quad (48)$$

$$\bar{B}_{15}(x) = \frac{\pi}{3} \sum_{s=1}^n \bar{Q}_{15}(r_{os}^3(x) - r_{is}^3(x)) \quad (49)$$

$$\bar{B}_{51}(x) = \frac{\pi}{3} \sum_{s=1}^n \bar{Q}_{51}(r_{os}^3(x) - r_{is}^3(x)) \quad (50)$$

$$\bar{B}_{61}(x) = \frac{2}{3}\pi \sum_{s=1}^n \bar{Q}_{61}(r_{os}^3(x) - r_{is}^3(x)) \quad (51)$$

$$\bar{D}_{11}(x) = \frac{\pi}{4} \sum_{s=1}^n \bar{Q}_{11}(r_{os}^4(x) - r_{is}^4(x)) \quad (52)$$

The strain energy  $U_{BS}$  in Equation (31) represents the strain energy of the composite shaft that results from the bending moment and the shear force, but when the composite shaft is subjected to a constant axial force, the total strain energy of the composite shaft  $U_{comp}$  is given by

$$U_{comp} = U_{BS} + U_F \quad (53)$$

where  $U_F$  is the external work done on the shaft due to a constant axial force  $P$  that can be written as

$$U_F = \frac{1}{2} \int_0^L P \left[ \left( \frac{\partial v}{\partial x} \right)^2 + \left( \frac{\partial w}{\partial x} \right)^2 \right] dx \quad (54)$$

### 3 Hierarchical composite shaft element formulation

The shape functions for hierarchical finite element can be established from polynomial or trigonometric functions. In this work the trigonometric function is chosen. Figure 3 illustrates a

hierarchical beam finite element for tapered composite shaft. The element has two nodes and each of them have four degrees of freedom (two translational and two rotational). In hierarchical finite element method, the transverse displacement field of the beam element in y-direction is expressed as

$$v = c_1 + c_2 \frac{x}{L} + \sum_{n=1}^N c_{n+2} \sin \frac{n\pi x}{L} \quad (55)$$

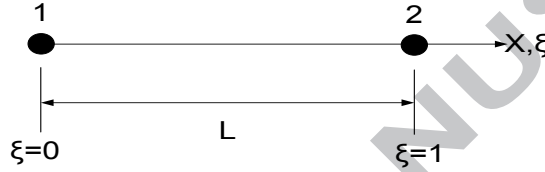


Figure 3 Hierarchical beam finite element with two nodes

The local coordinate  $x$  and non-dimensional coordinate  $\xi$  are related by

$$\xi = \frac{x}{L}, \quad 0 \leq \xi \leq 1 \quad (56)$$

So, Equation (55) can be written as

$$v = c_1 + c_2 \xi + \sum_{n=1}^N c_{n+2} \sin (n\pi \xi) \quad (57)$$

$$v = [1 \quad \xi \quad \sin \pi \xi \quad \dots \quad \sin N\pi \xi] \begin{bmatrix} c_1 \\ c_2 \\ c_3 \\ c_4 \\ \vdots \\ c_{N+2} \end{bmatrix} \quad (58)$$

$$v = [K^v]\{c\} \quad (59)$$

where N is the number of the hierarchical terms of displacement. In local coordinate system, the nodal displacements in y-direction are

$$\{q_v\} = \begin{bmatrix} v_1 \\ v_2 \\ v_3 \\ v_4 \\ \vdots \\ v_{N+2} \end{bmatrix} = \begin{bmatrix} 1 & 0 & 0 & 0 & 0 \\ 1 & L & 0 & 0 & 0 \\ 0 & 0 & 1 & 0 & 0 \\ 0 & 0 & 0 & 1 & \ddots & 0 \\ \vdots & \vdots & \vdots & \vdots & \ddots & \vdots \\ 0 & 0 & 0 & 0 & \vdots & 1 \end{bmatrix} \begin{bmatrix} c_1 \\ c_2 \\ c_3 \\ c_4 \\ \vdots \\ c_{N+2} \end{bmatrix} \quad (60)$$

$$\{q_v\} = [K^{q_v}]\{c\} \quad (61)$$

The displacement in y-direction can be expressed as

$$v = [f_1 \ f_2 \ f_3 \ f_4 \ \dots \ f_{N+2}] \begin{bmatrix} v_1 \\ v_2 \\ v_3 \\ v_4 \\ \vdots \\ v_{N+2} \end{bmatrix} \quad (62)$$

$$v = [N_v]\{q_v\} = f_1 v_1 + f_2 v_2 + \sum_{n=1}^N f_{n+2} v_{n+2} \quad (63)$$

Substituting Equations (59) and (61) into Equation (63)

$$[N_v]\{q_v\} = [N_v][K^{q_v}]\{c\} = [K^v]\{c\} \quad (64)$$

One can obtain the shape functions of the displacement  $v$  as:

$$[N_v] = [1 - \xi \ \xi \ \sin \pi \xi \ \sin 2\pi \xi \ \sin 3\pi \xi \ \dots \ \sin N\pi \xi] \quad (65)$$

where

$$f_1 = 1 - \xi \quad (66)$$

$$f_2 = \xi \quad (67)$$

$$f_{n+2} = \sin(n \pi \xi) \quad (68)$$

where  $N$  is the number of the hierarchical terms,  $n = 1, 2, 3, \dots, N$ .

The functions  $f_1$  and  $f_2$  are polynomial functions and they correspond to the nodal displacements of the hierarchical element, whilst functions  $f_{n+2}$  are trigonometric functions and they correspond to the hierarchical terms and contribute only to the internal field of the displacement and do not affect the nodal displacement. Repeating the previous procedure, one can obtain the shape functions for  $w$ ,  $\beta_y$  and  $\beta_z$ . As a result, the displacement vector formed by the variables  $v$ ,  $w$ ,  $\beta_y$  and  $\beta_z$  can be written as:

$$\begin{bmatrix} v \\ w \\ \beta_y \\ \beta_z \end{bmatrix} = \begin{bmatrix} [N_v] & [0] & [0] & [0] \\ [0] & [N_w] & [0] & [0] \\ [0] & [0] & [N_{\beta_y}] & [0] \\ [0] & [0] & [0] & [N_{\beta_z}] \end{bmatrix} \begin{bmatrix} \{q_v\} \\ \{q_w\} \\ \{q_{\beta_y}\} \\ \{q_{\beta_z}\} \end{bmatrix} \quad (69)$$

$$[N_{v,w,\beta_y,\beta_z}] = [f_1 \ f_2 \ f_3 \ \dots \ f_{N+2}] \quad (70)$$

$$\{q_v\} = \{v_1, v_2, v_3, \dots, v_{N+2}\}^T \quad (71)$$

$$\{q_w\} = \{w_1, w_2, w_3, \dots, w_{N+2}\}^T \quad (72)$$

$$\{q_{\beta_y}\} = \{\beta_{y1}, \beta_{y2}, \beta_{y3}, \dots, \beta_{y(N+2)}\}^T \quad (73)$$

$$\{q_{\beta_z}\} = \{\beta_{z1}, \beta_{z2}, \beta_{z3}, \dots, \beta_{z(N+2)}\}^T \quad (74)$$

Substituting Equation (69) into Equation (1), Equation (31), and Equation (54) and then applying the Lagrange's equations, one can get the equations of motion of free vibration of spinning tapered composite driveshaft. In addition to the number of the nodes, the number of the generalized co-ordinates depends on the number of the hierarchical terms. So, the generalized co-ordinates are

$$\begin{aligned}
 q_1 = v_1 & \quad q_2 = v_2 & \quad q_3 = v_3 & \quad \dots\dots & \quad q_b = v_{N+2} \\
 q_{b+1} = w_1 & \quad q_{b+2} = w_2 & \quad q_{b+3} = w_3 & \quad \dots\dots & \quad q_{2b} = w_{N+2} \\
 q_{2b+1} = \beta_{y1} & \quad q_{2b+2} = \beta_{y2} & \quad q_{2b+3} = \beta_{y3} & \quad \dots\dots & \quad q_{3b} = \beta_{y(N+2)} \\
 q_{3b+1} = \beta_{z1} & \quad q_{3b+2} = \beta_{z2} & \quad q_{3b+3} = \beta_{z3} & \quad \dots\dots & \quad q_{4b} = \beta_{z(N+2)}
 \end{aligned} \tag{75}$$

where  $b = N + 2$ . Also, the generalized co-ordinates can be expressed as

$$\{q\} = \begin{bmatrix} \{q_v\} \\ \{q_w\} \\ \{q_{\beta_y}\} \\ \{q_{\beta_z}\} \end{bmatrix} \tag{76}$$

After applying Lagrange's equations, the equations of motion of free vibration of rotating tapered composite driveshaft can be written as

$$[M]\{\ddot{q}\} + [G]\{\dot{q}\} + ([K] + [K_p])\{q\} = \{0\} \tag{77}$$

where

$$[M] = \begin{bmatrix} [M_{11}] & [0] & [0] & [0] \\ [0] & [M_{22}] & [0] & [0] \\ [0] & [0] & [M_{33}] & [0] \\ [0] & [0] & [0] & [M_{44}] \end{bmatrix} \tag{78}$$

$$[G] = \begin{bmatrix} [0] & [0] & [0] & [0] \\ [0] & [0] & [0] & [0] \\ [0] & [0] & [0] & [G_{34}] \\ [0] & [0] & [G_{43}] & [0] \end{bmatrix} \quad (79)$$

$$[K] = \begin{bmatrix} [K_{11}] & 0 & [K_{13}] & [K_{14}] \\ [0] & [K_{22}] & [K_{23}] & [K_{24}] \\ [K_{31}] & [K_{32}] & [K_{33}] & [K_{34}] \\ [K_{41}] & [K_{42}] & [K_{43}] & [K_{44}] \end{bmatrix} \quad (80)$$

$$[K_p] = \begin{bmatrix} [K_{pv}] & [0] & [0] & [0] \\ [0] & [K_{pw}] & [0] & [0] \\ [0] & [0] & [0] & [0] \\ [0] & [0] & [0] & [0] \end{bmatrix} \quad (81)$$

The mass sub-matrices, gyroscopic sub-matrices, and stiffness sub-matrices for tapered composite driveshaft using hierarchical finite element method are given in details in the Appendix A.

#### 4 Rayleigh - Ritz solution

To validate the solution from the hierarchical composite tapered shaft finite element model, Rayleigh – Ritz method is utilized here. It is developed to obtain an approximate solution for the tapered composite shaft. The simply supported condition at the ends of the tapered composite shaft is used to obtain the model, and the series solution functions are assumed for  $v$ ,  $w$ ,  $\beta_y$ , and  $\beta_z$  in the form

$$v = \bar{v}e^{i\omega t} \quad (82)$$

$$w = \bar{w}e^{i\omega t} \quad (83)$$

$$\beta_y = \bar{\beta}_y e^{i\omega t} \quad (84)$$

$$\beta_z = \bar{\beta}_z e^{i\omega t} \quad (85)$$

where

$$\bar{v}(x) = \sum_{j=1}^n V_j \sin \frac{j\pi x}{L} \quad (86)$$

$$\bar{w}(x) = \sum_{j=1}^n W_j \sin \frac{j\pi x}{L} \quad (87)$$

$$\bar{\beta}_y(x) = \sum_{j=1}^n B_{yj} \cos \frac{j\pi x}{L} \quad (88)$$

$$\bar{\beta}_z(x) = \sum_{j=1}^n B_{zj} \cos \frac{j\pi x}{L} \quad (89)$$

Here,  $n$  is the number of Ritz terms and  $\omega$  is whirl frequency. To obtain the equations of motion, Equations (82) - (85) must be substituted in Equation (1) and Equation (31) which represent the kinetic energy and the strain energy of the tapered composite shaft, respectively. After obtaining the energy expressions in terms of the series solution of  $v, w, \beta_y$  and  $\beta_z$ , Lagrange's equations can be used to establish the equations of motion of the tapered composite shaft. The equations of motion of free vibration of the rotating tapered composite shaft are

$$[M_r]\{\ddot{q}\} + [G_r]\{\dot{q}\} + [K_r]\{q\} = \{0\} \quad (90)$$

Where

$$[M_r] = \begin{bmatrix} [M_V]_{n \times n} & [0]_{n \times n} & [0]_{n \times n} & [0]_{n \times n} \\ [0]_{n \times n} & [M_W]_{n \times n} & [0]_{n \times n} & [0]_{n \times n} \\ [0]_{n \times n} & [0]_{n \times n} & [M_{B_y}]_{n \times n} & [0]_{n \times n} \\ [0]_{n \times n} & [0]_{n \times n} & [0]_{n \times n} & [M_{B_z}]_{n \times n} \end{bmatrix} \quad (91)$$

$4n \times 4n$

$$[G_r] = \begin{bmatrix} [0]_{n \times n} & [0]_{n \times n} & [0]_{n \times n} & [0]_{n \times n} \\ [0]_{n \times n} & [0]_{n \times n} & [0]_{n \times n} & [0]_{n \times n} \\ [0]_{n \times n} & [0]_{n \times n} & [0]_{n \times n} & [G_{B_z}]_{n \times n} \\ [0]_{n \times n} & [0]_{n \times n} & [G_{B_y}]_{n \times n} & [0]_{n \times n} \end{bmatrix} \quad (92)$$

$4n \times 4n$

$$[K_r] = \begin{bmatrix} [K_{V1}]_{n \times n} & [0]_{n \times n} & [K_{V3}]_{n \times n} & [K_{V4}]_{n \times n} \\ [0]_{n \times n} & [K_{W2}]_{n \times n} & [K_{W3}]_{n \times n} & [K_{W4}]_{n \times n} \\ [K_{B_y1}]_{n \times n} & [K_{B_y2}]_{n \times n} & [K_{B_y3}]_{n \times n} & [K_{B_y4}]_{n \times n} \\ [K_{B_z1}]_{n \times n} & [K_{B_z2}]_{n \times n} & [K_{B_z3}]_{n \times n} & [K_{B_z4}]_{n \times n} \end{bmatrix} \quad (93)$$

$4n \times 4n$

$$\{q\} = \{V_1, V_2, \dots, V_n \quad W_1, W_2, \dots, W_n \quad B_{y1}, B_{y2}, \dots, B_{yn} \quad B_{z1}, B_{z2}, \dots, B_{zn}\}^T \quad (94)$$

The mass sub-matrices, gyroscopic sub-matrices, and stiffness sub-matrices for tapered composite driveshaft using Rayleigh - Ritz method are given in details in the Appendix B.

## 5 Campbell Diagram and Critical Speeds

Synchronous force or excitation is defined as the force, whose frequency is like rotor speed.

Mostly, the synchronous excitation happens because of the mass unbalance and disk skew [13].

Thus, under synchronous force or excitation equation (77) can be written as

$$[M]\{\ddot{q}\} + [G]\{\dot{q}\} + ([K] + [K_p])\{q\} = \{Q\} \quad (95)$$

where  $\{Q(t)\}$  represents the resulting forces and moments of the mass unbalance and the disk skew.

Moreover, Campbell diagram is a map of natural frequencies of the driveshaft that shows the variation of the natural frequencies with the rotation speeds; the Campbell diagram is used to obtain the critical speeds and natural frequencies. Figure 14 shows a typical Campbell diagram where the intersections of the natural frequency curve with the forcing frequency lines represent the critical speeds. In addition, beside the Campbell diagram, there are two other methods to obtain the critical speeds; one is called the direct method and the other is the iteration method. In this paper, the direct method is applied. The critical speeds are taken when one of the natural frequencies at a specific speed is equal to the forcing frequency [13]. The forcing frequency can be written in terms of rotational speed as

$$\omega_f = n\Omega \quad (96)$$

where  $n$  refers to the level of the lateral force on the shaft. For example, in out of balance  $n = 1$  and in a four bladed helicopter rotor  $n = 4$ . In Equation (95) the force is in form  $\{Q(t)\} = \{Q_0\} e^{j\omega_f t}$ , so the solutions of equation (95) will be in form  $\{q(t)\} = \{q_0\} e^{j\omega_f t}$

$$(-\Omega^2[n^2[M] + jn[G]] + j\Omega n [C] + ([K] + [K_p])) \{q_0\} = \{Q_0\} \quad (97)$$

By putting  $\{Q_0\} = \{0\}$  in equation (96), one can get

$$(-\Omega^2[n^2[M] + jn[G]] + j\Omega n [C] + ([K] + [K_p])) \{q_0\} = \{0\} \quad (98)$$

The solution of eigenvalue problem  $\Omega$  is in complex form; the real part of  $\Omega$  gives the critical speed.

It is noted here that the value of the shear correction factor ( $k_s$ ) is determined using the following equation that is available in Reference [15].

$$k_s = \frac{6 E_{xx} (1 - \bar{m}^4)(1 + \bar{m}^2)}{G_{xz} v_{xz} (2\bar{m}^6 + 18\bar{m}^4 - 18\bar{m}^2 - 2) - E_{xx}(7\bar{m}^6 + 27\bar{m}^4 - 27\bar{m}^2 - 7)} \quad (99)$$

where

$$\bar{m} = \bar{r} / \bar{R} \quad (100)$$

where  $\bar{r}$  is the mean inner radius and  $\bar{R}$  is the mean outer radius of the hollow tapered composite shaft.

This equation from Reference [15] gives different values of  $k_s$  based on different values of  $\bar{m}$  for the tapered shafts made of the same composite material. Therefore, because tapered shafts of different inner radius and outer radius values are used in the numerical examples given in different sections of the paper in the following, correspondingly, the value of  $k_s$  for each numerical example is different depending on the  $\bar{m}$  value of the shaft of that particular numerical example.

## 6 Validation

To validate the new hierarchical finite element model, a tapered composite shaft made of graphite-epoxy material is considered. The shaft is simply supported at the ends, and the outer diameter of the composite shaft at the right end increases with increasing the tapered shaft length; Figure 4 shows the graphite-epoxy tapered shaft with two bearings at both ends. The material properties and geometric dimensions of the tapered composite shaft are given in Table 1 and Table 2, respectively. The outer and the inner diameters in Table 2 represent the diameters of the shaft at the right end as it is shown in Figure 4.

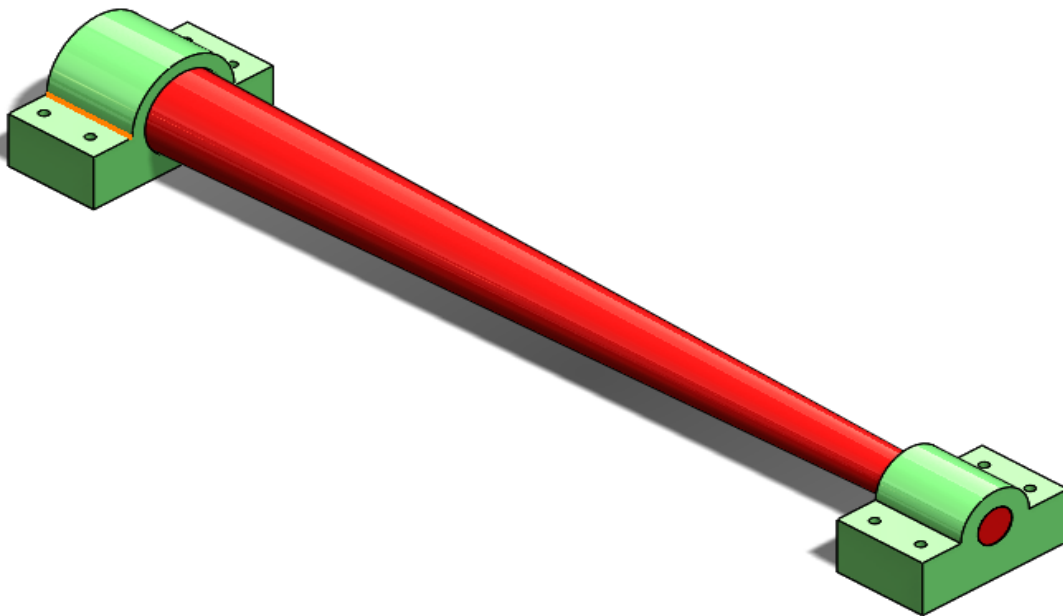


Figure 4 The configuration of the tapered graphite - epoxy composite shaft

Table 1 Properties of the composite material [2]

Properties	Boron-epoxy	Graphite-epoxy
$E_{11}$ (GPa)	211	139
$E_{22}$ (GPa)	24	11
$G_{12} = G_{13}$ (GPa)	6.9	6.05
$G_{23}$ (GPa)	6.9	3.78
$\nu_{12}$	0.36	0.313
Density (Kg/m <sup>3</sup> )	1967	1578

Table 2 The geometric dimensions and properties of the tapered composite shaft

Composite Shaft				
Length, $L = 2.47$ m	Inner Diameter,  ID = 0.1243m	Outer Diameter,  OD = 0.1269 m	Lay-up from inside  [90/45/-45/0 <sub>6</sub> /90]	Shear correction factor, $k_s =$ 0.503

The natural frequencies of the tapered composite shaft for different taper angles are calculated using the hierarchical finite element model. The results are given in Table 3, and they are listed with those obtained using Rayleigh-Ritz solution. It can be seen from Table 3 that the difference is small between the present model and Rayleigh-Ritz solution in obtaining the natural frequencies. In addition, it can be observed from the table that the natural frequencies increase with increasing the taper angle; for example, at 0° of taper angle the first forward natural frequency is 666 Hz and when the taper angle increases to 2° and 3°, the first forward natural frequency increases by 25% and 40%, respectively. This increase in the natural frequencies happens because the circumference of the cross-section increases through the length of the shaft from the left end to the right end when increasing the taper angle. This means the amount of composite material increases through the length of the shaft when increasing the taper angle, which makes the tapered composite shaft stiffer

than the uniform composite shaft. In this analysis six elements of equal lengths and ten hierarchical terms were used for the hierarchical finite element model while for Rayleigh-Ritz solution five Ritz terms were enough for convergence.

In addition, Table 4 shows the first critical speeds of the tapered composite shaft for different taper angles, and a good agreement between the results calculated using the hierarchical finite element model and the Rayleigh-Ritz solution can be observed.

In addition, a numerical example of hollow tapered shaft made of homogeneous isotropic material is presented here. Figure 5 shows the hollow tapered shaft and it is simply supported at the ends. At the right end of the tapered shaft, as illustrated in Figure 5, the inner and outer diameters are 0.05 m and 0.1 m respectively, and the length is 1 m. The taper angle of the shaft is chosen to be  $15^\circ$ . The Young's modulus, mass density, and Poisson's ratio are taken to be 200 GPa, 7810 Kg/m<sup>3</sup>, and 0.3 respectively. Four equal-length elements with 10 hierarchical terms are considered for this analysis. The first natural frequency of the tapered shaft at 10000 RPM is presented in Table 5 along with the results obtained in Ref. [14]. The present results show good agreement with the results given in Ref. [14].

Table 3 The natural frequencies in Hz of the tapered composite shaft at 10000 rpm with different taper angles obtained using finite element method and Rayleigh-Ritz method.

Taper angle	Mode	Hierarchical finite element	Rayleigh-Ritz method
0°	BW1	664	663.76
	FW1	666	666.10
	BW2	2170	2168.3
	FW2	2176	2172.6
1°	BW1	758	759.96
	FW1	761	762.93
	BW2	2370	2369
	FW2	2375	2373.4
2°	BW1	830	839
	FW1	834	843
	BW2	2513	2517
	FW2	2519	2522
3°	BW1	885	905.40
	FW1	890	909.63
	BW2	2618	2630
	FW2	2625	2635

Table 4 First critical speed in rpm of the tapered composite shaft with different taper angles using finite element method and Rayleigh-Ritz method

Taper angle, degrees	Hierarchical Finite element	Rayleigh-Ritz method
0	39626	39617
1	45160	45285
2	49344	49901
3	52447	53765

Table 5 First natural frequency in Hz at 10000 RPM for a shaft made of an isotropic material

Frequency mode	Hierarchical Finite element	Ref. [14]	Difference %
FW	422	442.54	4.7
BW	416	395.35	5

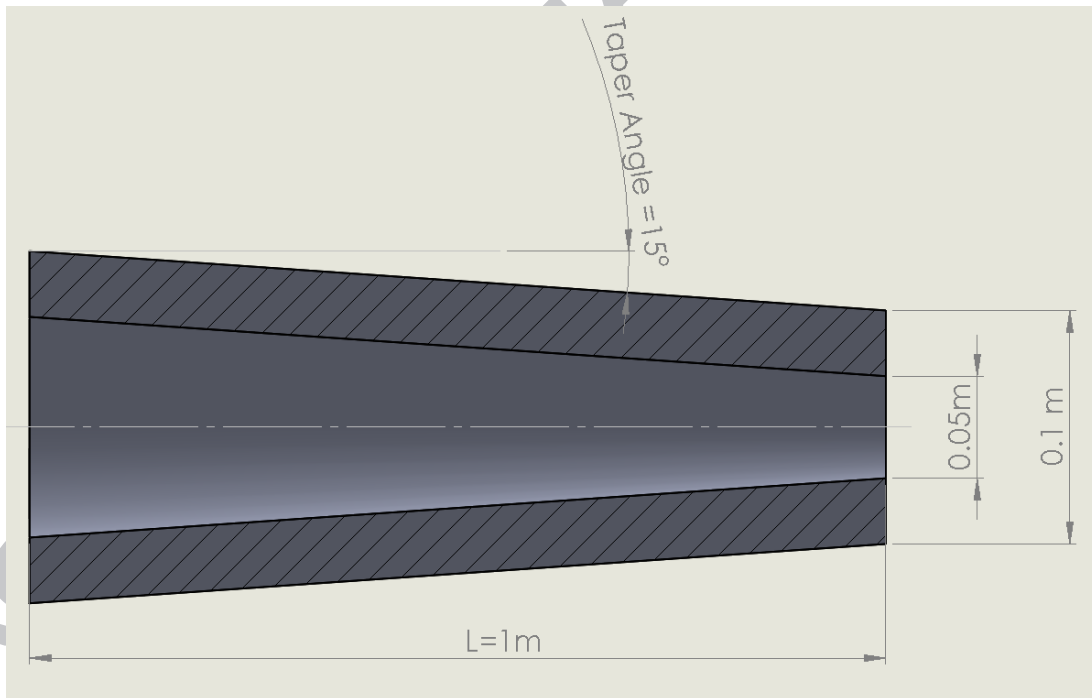


Figure 5 Hollow tapered shaft made of isotropic material

## 7 Numerical examples

In the section 3, the hierarchical finite element model was established for vibration analysis of the tapered composite shaft. It is important to assess the models in terms of its ability to predict the natural frequencies and the critical speeds of the tapered composite shaft, so in the previous section the finite element model was validated using Rayleigh-Ritz formulation and a good agreement between these models was observed.

Therefore, the hierarchical finite element model is credible enough to perform rotordynamic analysis and to study the effects of different parameters, such as the taper angle, fiber orientation, and axial load, on the natural frequencies and the critical speeds of the tapered composite shaft. Herein, three cases of the tapered composite shaft are considered to perform rotordynamic analysis; the effects of different parameters, such as the taper angle, fiber orientation, and axial load, on the natural frequencies and the critical speeds of these two tapered composite shafts are studied in this section.

### 7.1 Tapered Composite Shaft-Disk System Case A

In this section, rotordynamic analysis of tapered composite shaft-disk system is performed using the hierarchical finite element model. The tapered composite shaft has a disk at its middle and two bearings at the ends; the configuration of the tapered composite shaft is illustrated in Figure 6. The shaft is made of a graphite-epoxy composite material, and the geometric properties of the composite shaft are given in Table 6. Different taper angles are considered in the analysis. The inner and outer diameters at the right end of the shaft do not change with changing the taper angle, while at the left end they increase when increasing the taper angle. The tapered composite

shaft is modeled by eight elements of equal length using the hierarchical finite element model, respectively.

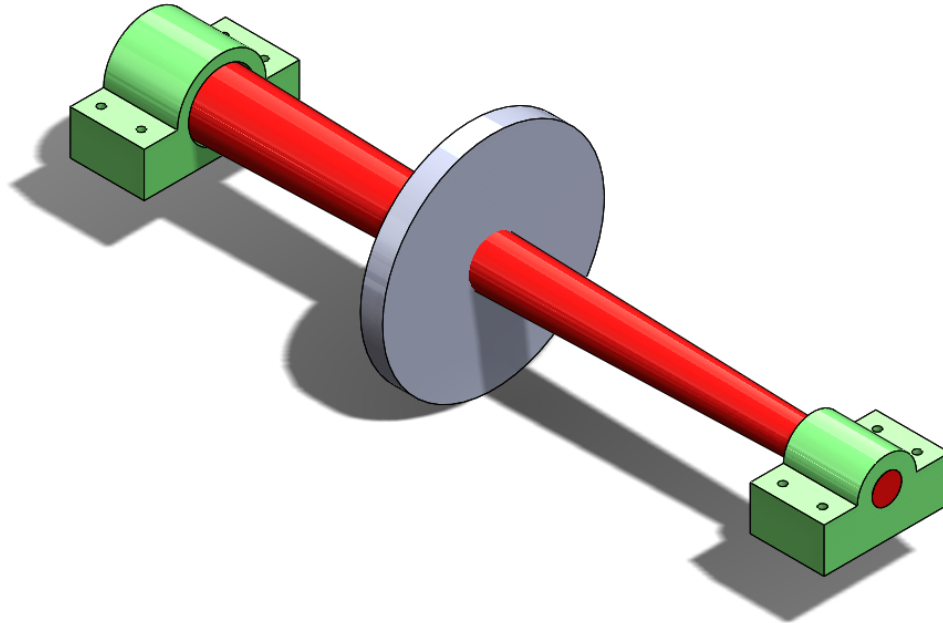


Figure 6 The configuration of the tapered graphite - epoxy composite shaft

Table 6 The geometric dimensions and properties of the tapered composite shaft

<b>Composite Shaft</b>				
$L = 0.72$ m	$ID = 0.028$ m	$OD = 0.048$ m	Lay-up from inside [90/45/-45/0 <sub>6</sub> /90]	Shear correction factor, $k_s = 0.56$
<b>Disk</b>				
Mass, $m = 2.4364$ Kg	Diametral mass moment of inertia, $I_d = 0.1901$ Kg.m <sup>2</sup>		Polar mass moment of inertia, $I_p = 0.3778$ Kg.m <sup>2</sup>	
<b>Bearing</b>				
$K_{yy} = K_{zz} = 17.5$ MN/m			$C_{zz} = C_{yy} = 500$ N.s/m	

Table 7 shows the first critical speeds of the tapered composite shaft for different taper angles, and it can be seen from the table that the first critical speed increases when increasing the taper angle. However, Figure 7 shows that the increase in the first critical speed when increasing the taper angle does not continue because the first critical speed reaches its maximum at  $10^\circ$  taper angle and then starts to drop off when increasing the taper angle; to understand why this happens, one needs to return to Equations (44) – (52) and to look at Figure 7. The equations represent the  $\overline{ABD}$  matrix that depends on the stiffness and the radius of the layer. Whereas, Figure 8 – Figure 11 represent the material stiffnesses for each single layer of the tapered composite shaft; from the figures it is clear that  $\overline{Q}_{11}$  is much higher than  $\overline{Q}_{15}$ ,  $\overline{Q}_{16}$ ,  $\overline{Q}_{55}$  and  $\overline{Q}_{66}$  for all the layers and the taper angles, and  $\overline{Q}_{11}$  decreases with increasing the taper angle except for the layer with fiber orientation of  $90^\circ$ . Consequently, in Figure 7 the inner and the outer radii of the layer control the first critical speed for taper angle of  $0^\circ \leq \alpha \leq 10^\circ$  while  $\overline{Q}_{11}$  controls the first critical speed for taper angle of  $10^\circ < \alpha \leq 20^\circ$ .

Table 7 The first critical speed in rpm of the tapered composite shaft for different taper angles.

Taper angle	Hierarchical finite element
$0^\circ$	7295
$1^\circ$	90710
$2^\circ$	11467
$3^\circ$	12820
$4^\circ$	13855

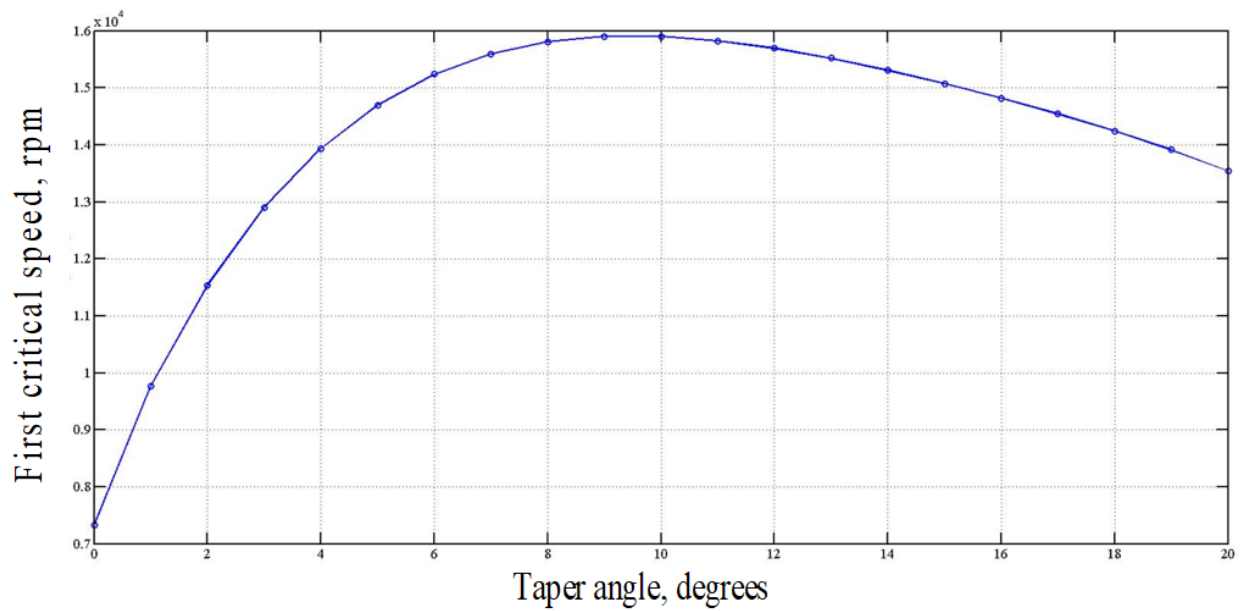


Figure 7 The first critical speeds of the tapered composite shaft for different taper angles determined using Hierarchical finite element model

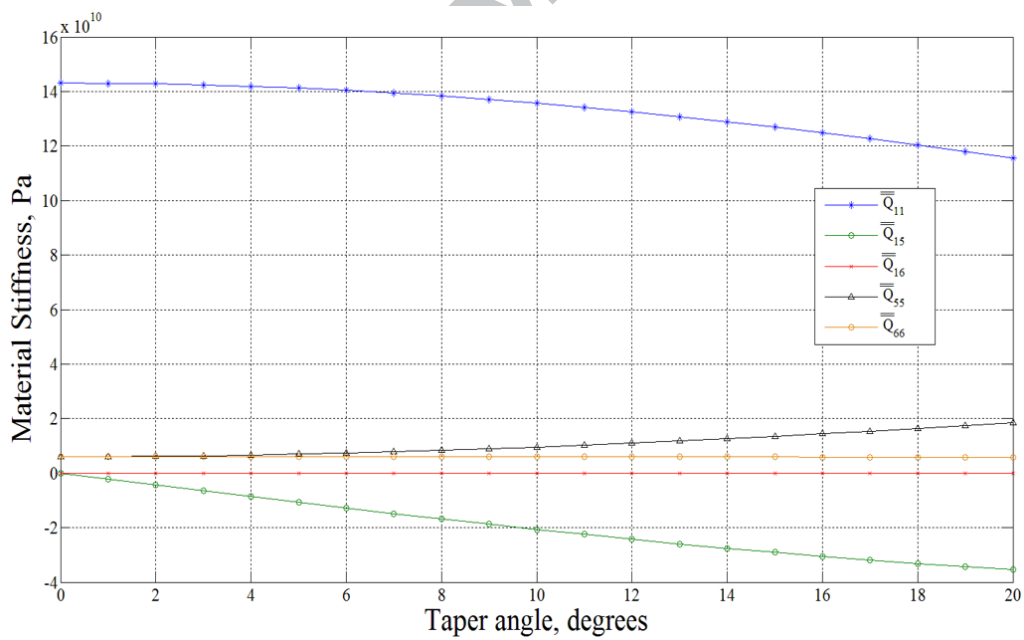


Figure 8  $\bar{Q}_{11}$ ,  $\bar{Q}_{15}$ ,  $\bar{Q}_{16}$ ,  $\bar{Q}_{55}$ , and  $\bar{Q}_{66}$  for the layer of graphite-epoxy with fiber orientation angle of 0°

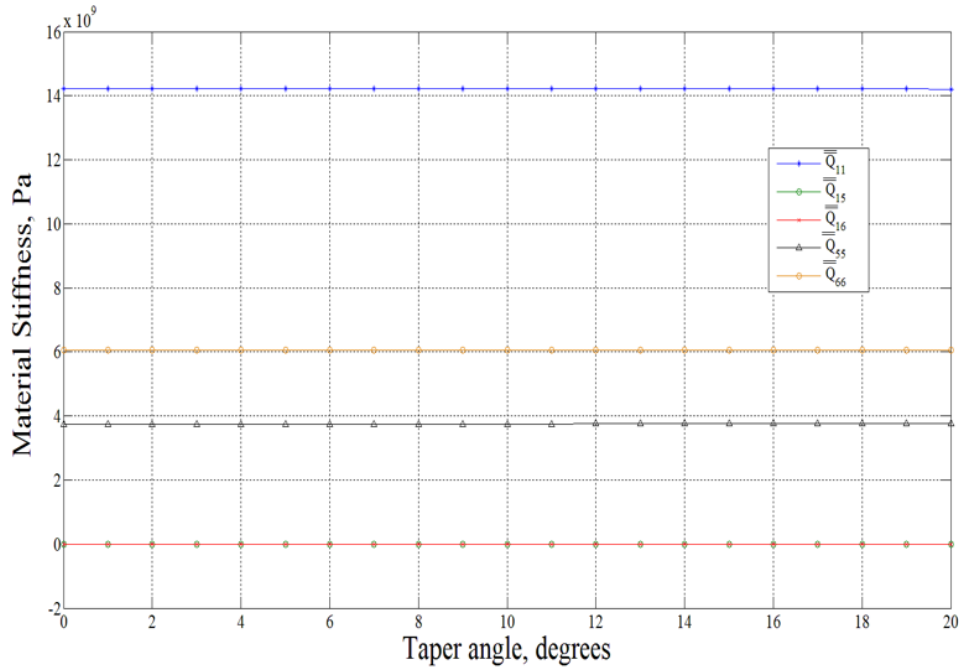


Figure 9  $\bar{Q}_{11}$ ,  $\bar{Q}_{15}$ ,  $\bar{Q}_{16}$ ,  $\bar{Q}_{55}$ , and  $\bar{Q}_{66}$  for the layer of graphite-epoxy with fiber orientation angle of 90°

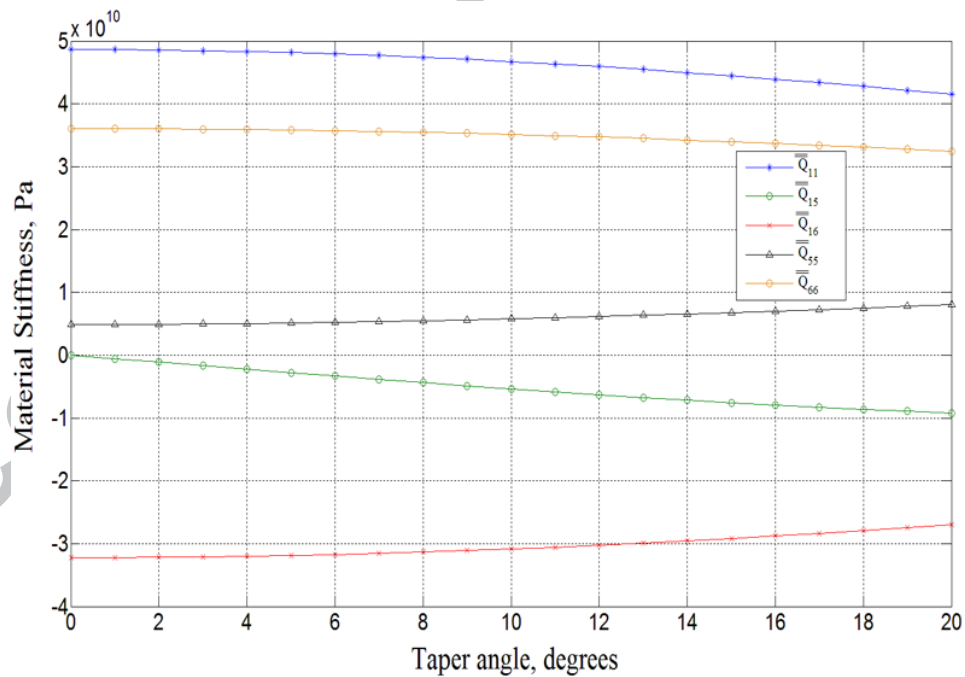


Figure 10  $\bar{Q}_{11}$ ,  $\bar{Q}_{15}$ ,  $\bar{Q}_{16}$ ,  $\bar{Q}_{55}$ , and  $\bar{Q}_{66}$  for the layer of graphite-epoxy with fiber orientation angle of 45°

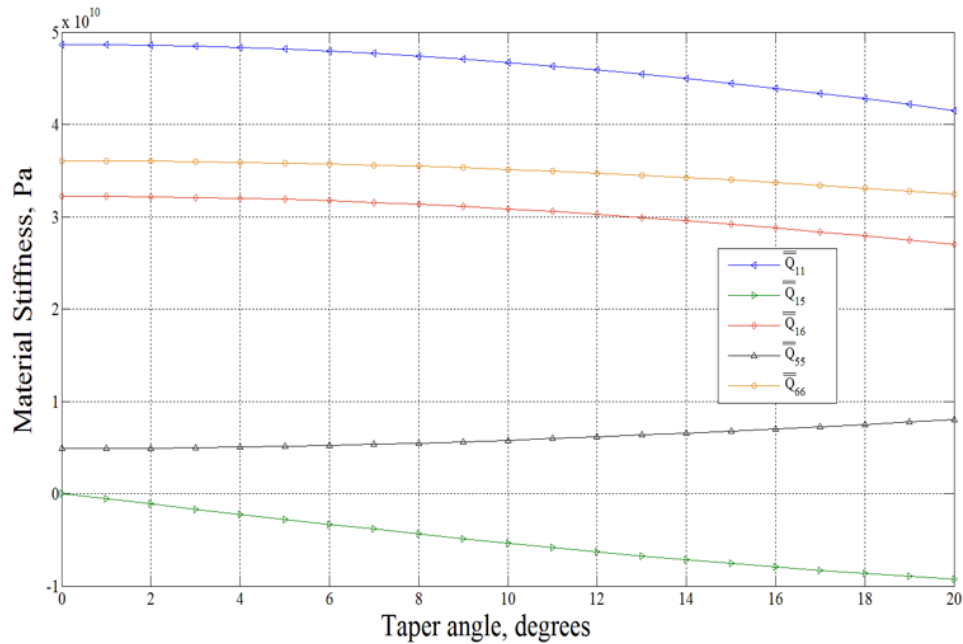


Figure 11  $\bar{Q}_{11}$ ,  $\bar{Q}_{15}$ ,  $\bar{Q}_{16}$ ,  $\bar{Q}_{55}$ , and  $\bar{Q}_{66}$  for the layer of graphite-epoxy with fiber orientation angle of  $-45^\circ$

### 7.1.1 Effect of The Disk Position on First critical speed

Moreover, the effect of the disk position on the first critical speed is studied. Figure 12 shows the tapered composite shaft with different disk positions. Table 8 illustrates the first critical speed of the tapered composite shaft for different disk positions and taper angles. For taper angles of  $0^\circ$  and  $1^\circ$  the maximum value of the first critical speed happens when the position of the disk is located at the center, while for taper angles between  $2^\circ$  and  $4^\circ$  the maximum value of the critical speed happens when the disk is located at  $4L/10$  from the left end. It can be said for high taper angles that the critical speed reaches its maximum as the disk approaches the left bearing where the inner and outer diameters are smaller than that at the right end.

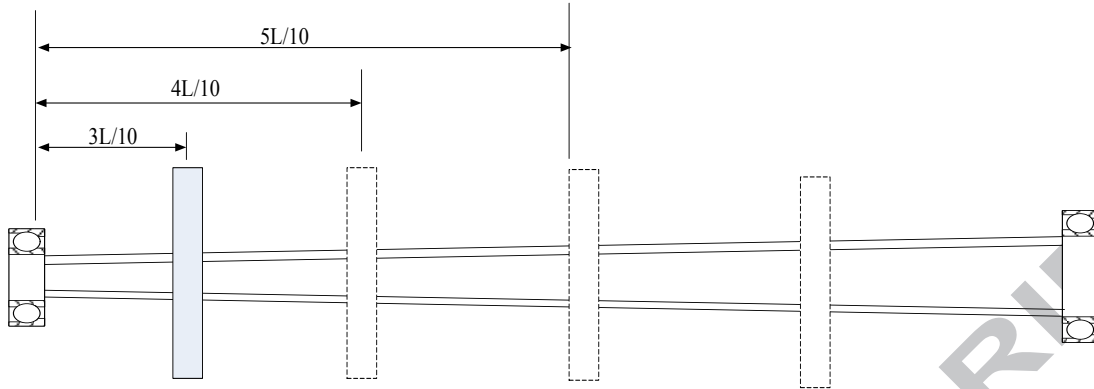


Figure 12 Tapered composite shaft with different positions of the disk.

Table 8 First critical speed in rpm of the tapered composite shaft for different taper angles and positions of the disk

Taper angle, degrees	The position of the disk				
	3L/10	4L/10	5L/10	6L/10	7L/10
0	5748	6602	7328	6602	5748
1	8144	9570	9760	8889	8159
2	10448	12011	11537	10829	10273
3	12532	13511	12903	12405	12033
4	14224	14408	13935	13639	13440
5	15285	15002	14699	14573	14527

### 7.1.2 Layers Stacking Sequence Effect

Furthermore, the effect of the stacking sequence of the layers on the first critical speed of the tapered composite shaft is analyzed. Table 9 illustrate the first critical speed for different stacking sequences and taper angles. The lay-up for the layers starts from inside, and there are ten layers with four different fiber orientation angles.

The layers near the outer surface have larger circumferences and volumes than those near the inner surface of the shaft, and they resist more bending moment than those layers that near form the inner surface; as a result, the outer surface layers control the stiffness of the shaft.

Consequently, it can be observed from Table 9 that laying up the layers that have high stiffness near the outer side of the shaft increases the critical speed. For example, at a taper angle of  $4^\circ$ , the first critical speed of the configuration  $[0_6^\circ/90^\circ/45^\circ/-45^\circ/90^\circ]$  is 13474 rpm, and in this configuration the layers that have fiber orientation of  $0^\circ$  are laid up on the inner side of the shaft. The layers with fiber orientation of  $0^\circ$  have higher stiffness than other layers, so laying up them near the outer surface increases the critical speed. Thus, the configuration  $[90^\circ/45^\circ/-45^\circ/90^\circ/0_6^\circ]$ , where the layers with  $0^\circ$  fiber orientation are laid-up on the outer side of the shaft, has higher first critical speed than the other configurations in Table 9. Moreover, it can be observed from the Table that the difference between the first critical speeds of the configurations A and E decreases when increasing the taper angle; for example, at  $0^\circ$ ,  $2^\circ$ , and  $4^\circ$  the differences in first critical speeds between the configurations A and E are 19%, 9.4%, and 5.1%, respectively. This is an indication that increasing the taper angle eliminates to some extent the effect of stacking sequence on the first critical speed and the natural frequencies.

Table 9 The first critical speed in rpm of the tapered composite shaft for different taper angles and stacking sequences determined using hierarchical finite element model

Configuration	Stacking sequence	Taper angle, degrees				
		$0^\circ$	$1^\circ$	$2^\circ$	$3^\circ$	$4^\circ$
A	$[0_6^\circ/90^\circ/45^\circ/-45^\circ/90^\circ]$	6456	8920	10787	12265	13418
B	$[90^\circ/0_6^\circ/45^\circ/-45^\circ/90^\circ]$	6798	9260	11099	12538	13653
C	$[90^\circ/45^\circ/0_6^\circ/-45^\circ/90^\circ]$	7032	9477	11278	12676	13751
D	$[90^\circ/45^\circ/-45^\circ/0_6^\circ/90^\circ]$	7295	9710	11467	12820	13855
E	$[90^\circ/45^\circ/-45^\circ/90^\circ/0_6^\circ]$	7668	10059	11776	13084	14078

### 7.1.3 Campbell Diagram and Mode Shape

In addition, Figure 13 – Figure 18 illustrate the mode shapes and Campbell diagrams for the tapered composite shaft with configuration of  $[90^\circ/45^\circ/-45^\circ/0_6^\circ/90^\circ]$  for three different taper angles. It can be observed that increasing the taper angle increases the natural frequency and affects the mode shape. These figures were obtained using the hierarchical finite element model.

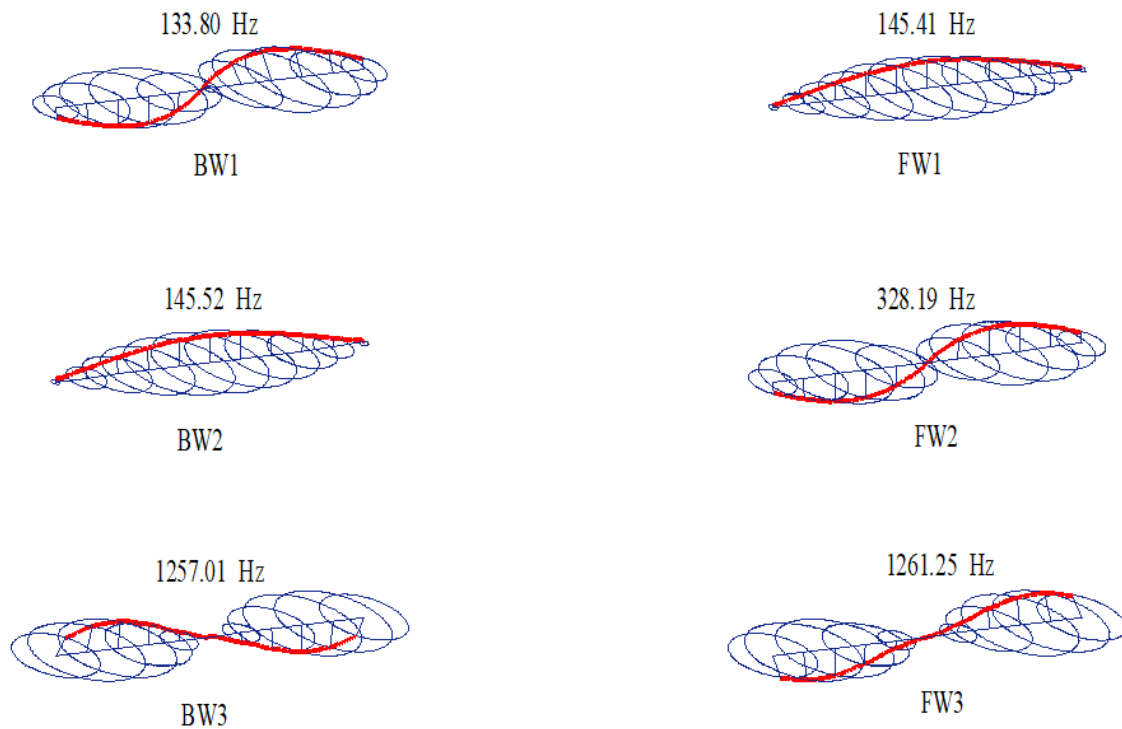


Figure 13 The mode shapes of the tapered composite shaft with taper angle of  $0^\circ$  at 6000 rpm

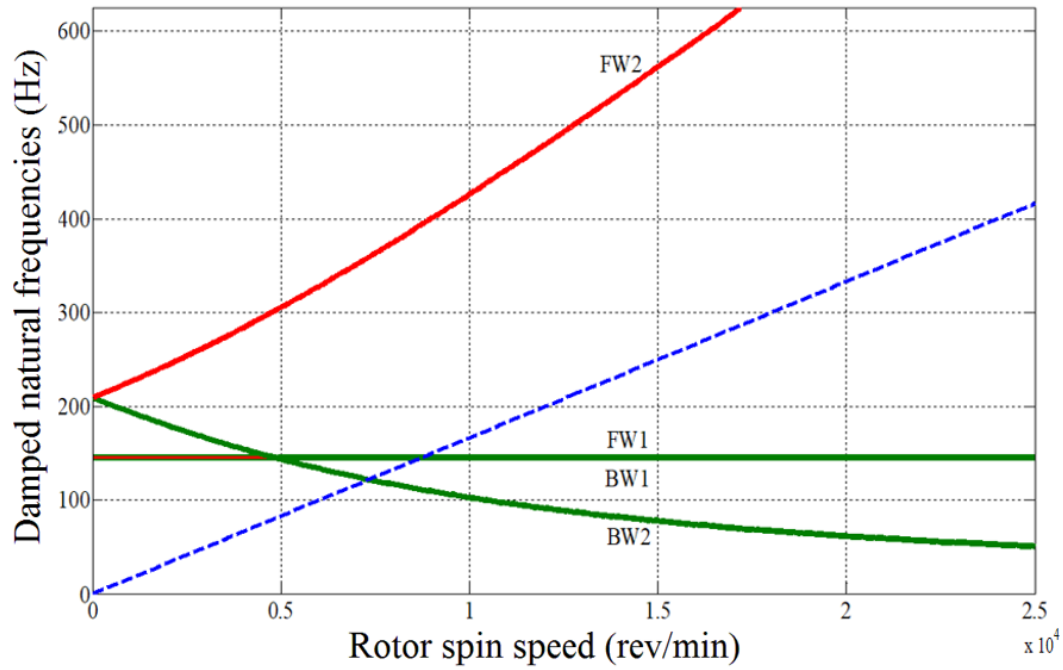


Figure 14 Campbell diagram of the tapered composite shaft with taper angle of  $0^\circ$ .

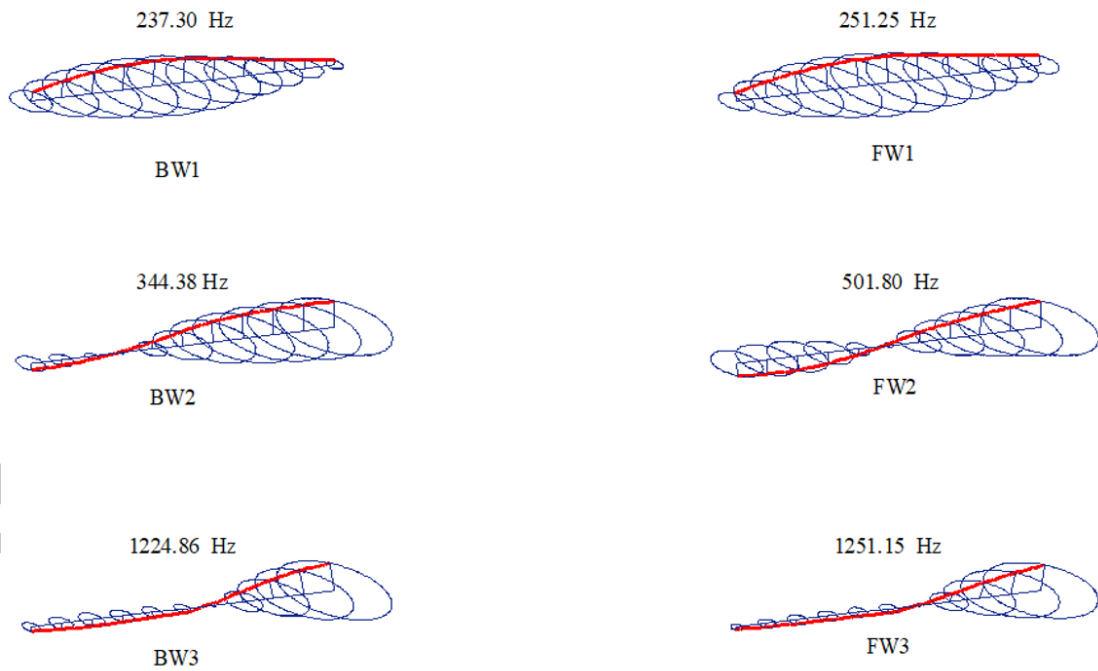


Figure 15 The mode shapes of the tapered composite shaft with taper angle of  $3^\circ$  at 6000 rpm

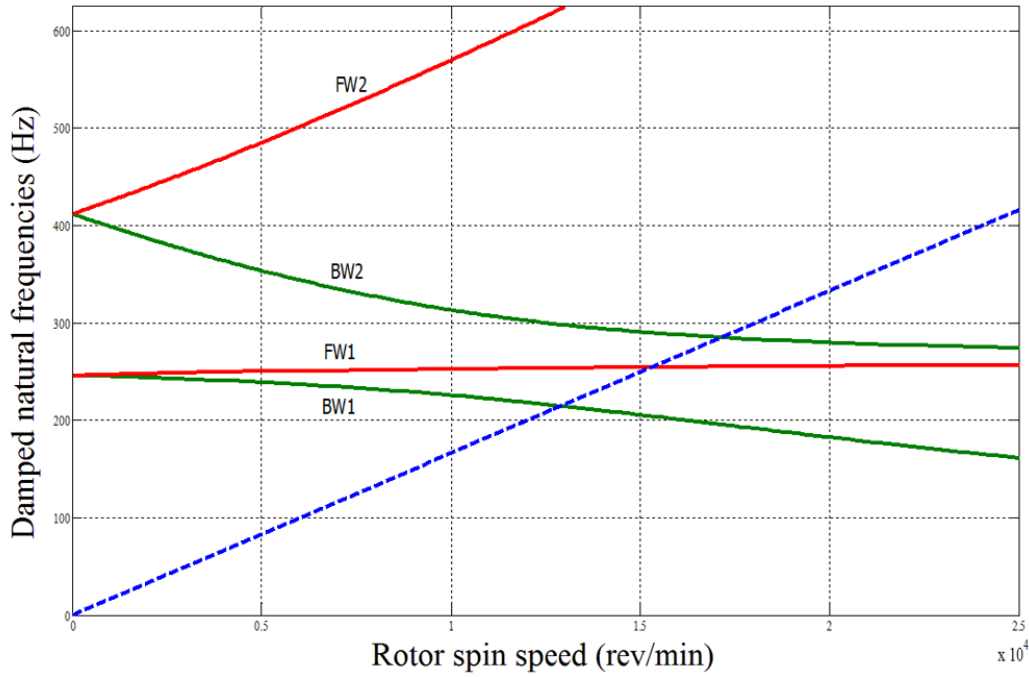


Figure 16 Campbell diagram of the tapered composite shaft with taper angle of 3°.

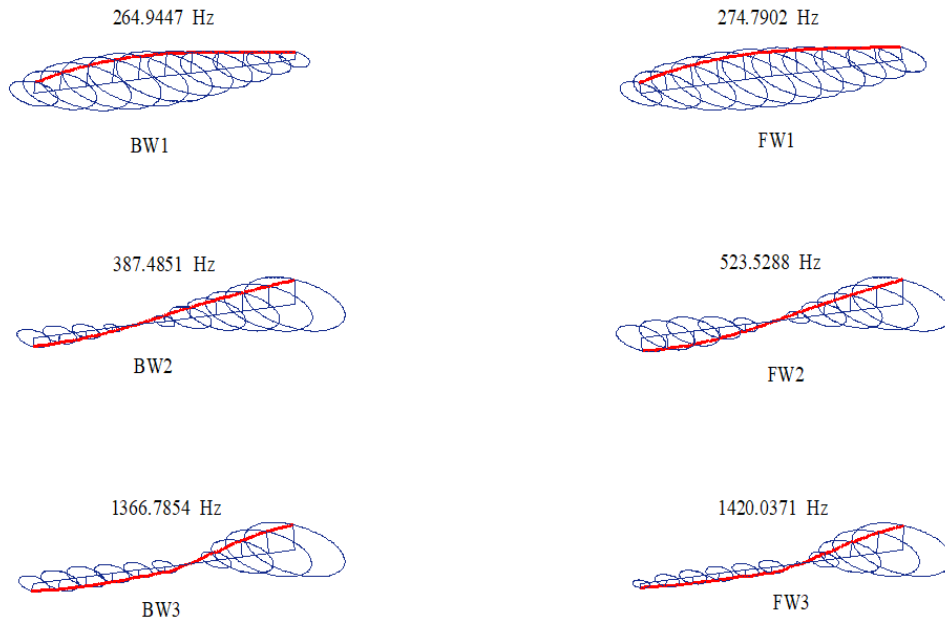


Figure 17 The mode shapes of the tapered composite shaft with taper angle of 5° at 6000 rpm

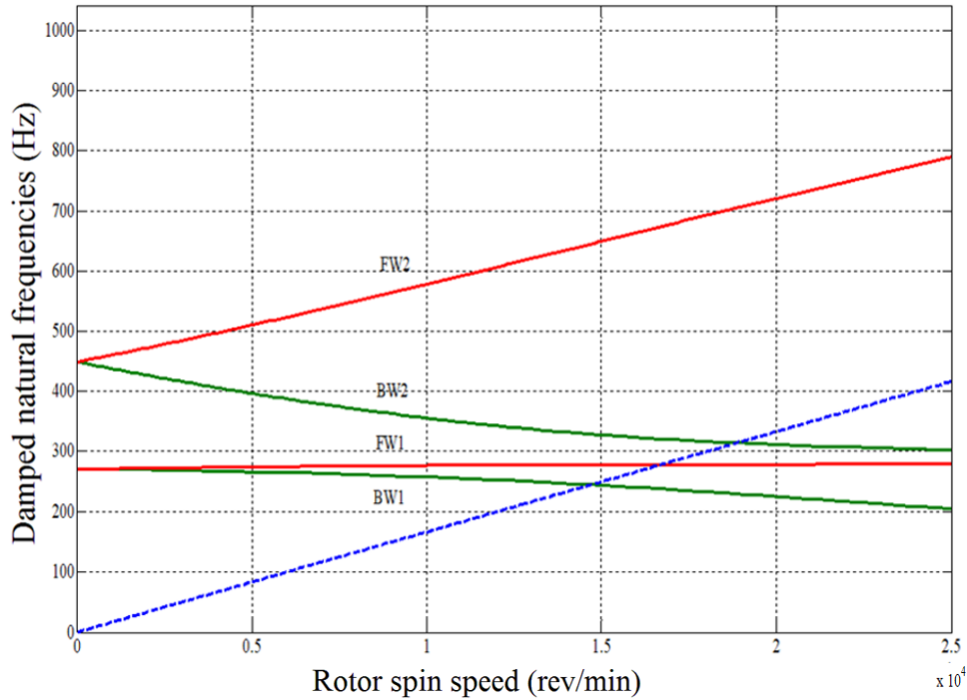


Figure 18 Campbell diagram of the tapered composite shaft with taper angle of 5°.

## 7.2 Tapered composite shaft Case B

In the following example, vibration of a tapered composite shaft subjected to different effects is studied. The tapered composite shaft is fixed by a bearing at one end and is free at the other end. The shaft is made of boron-epoxy composite material, and the properties of the composite material are listed in Table 1. The tapered composite shaft is made of ten layers, and the thickness of each layer is 0.025 mm. Also, the length of the shaft  $L$  is 0.5 m and the inner diameter  $d_i$  at the free end is 1 cm. Seven elements of equal length are considered for the analysis. The value of the shear correction factor  $k_s$  is calculated as explained before and is taken to be 0.5 for the shafts of all sub-cases considered in the following.

### 7.2.1 Effect of length on natural frequencies and first critical speed

In this section, the effect of the length on the natural frequencies and first critical speed of the tapered composite shaft is discussed. Figure 19 shows the configuration of the tapered composite shaft with different lengths. The length of the tapered composite shaft changes from  $L$  to  $0.7L$  by 10 percent every time, and the natural frequencies and critical speeds were obtained for different taper angles for each length. The inner diameter at the free end of the tapered composite shaft is kept at 1 cm, whereas the inner diameter of the other end changes with the changing taper angle and length. The stiffness of the bearings  $K_{yy}$  and  $K_{zz}$  are 10 GN/m. The configuration of the tapered composite shaft is  $[90^\circ/45^\circ/-45^\circ/0_6^\circ/90^\circ]$  and the lay-up starts from inside. Table 10 shows the natural frequencies of the tapered composite shaft with different lengths and taper angles. Two rotational speeds, 0 rpm and 5,000 rpm, are considered to calculate the natural frequencies. One can observe from the table that the natural frequencies increase when the length decreases or when the taper angle increases.

Furthermore, Table 10 shows that, in this example, the gyroscopic effect does not influence the natural frequency. For instance, the first backward natural frequency at 0 rpm and 5,000 rpm are almost the same for all taper angles. The natural frequencies in Table 10 are obtained using the hierarchical finite element. Moreover, Figure 20 shows the first critical speeds obtained using the hierarchical finite elements. From the figures, the difference between the first critical speeds increases with an increasing taper angle.

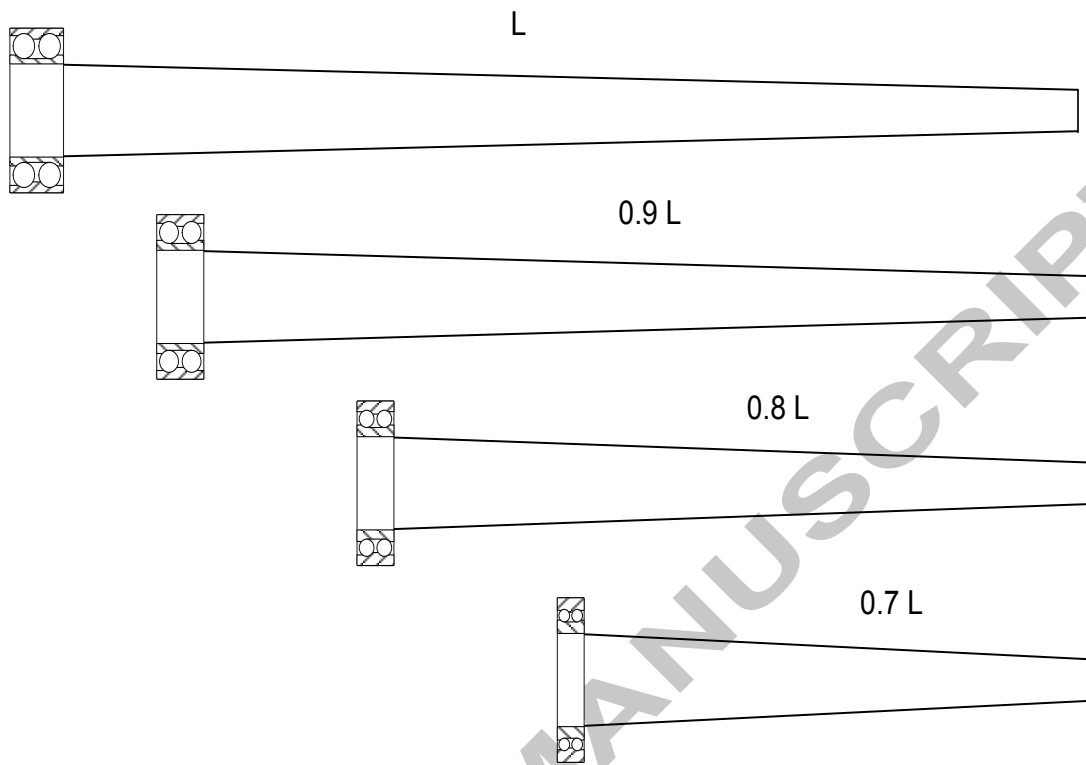


Figure 19 Different lengths of the tapered composite shaft.

Table 10 Natural frequencies in Hz of the tapered composite shaft with different lengths

Length, m	Rotational speed (rpm)	Mode	Taper angle, degrees					
			0°	1°	2°	3°	4°	5°
L = 0.5	0	BW1	416	737	1235	1272	1483	1658
		FW1	416	737	1235	1272	1483	1658
	5000	BW1	415	737	1022	1271	1482	1657
		FW1	416	738	1024	1273	1484	1660
0.9 L	0	BW1	511	864	1175	1444	1672	1860
		FW1	511	864	1175	1444	1672	1860
	5000	BW1	511	864	1175	1444	1671	1859
		FW1	512	865	1177	1446	1673	1862
0.8 L	0	BW1	644	1035	1376	1669	1914	2118
		FW1	644	1035	1376	1669	1914	2118
	5000	BW1	644	1034	1375	1667	1913	2117
		FW1	644	1036	1377	1669	1915	2120
0.7 L	0	BW1	835	1272	1648	1968	2236	2458
		FW1	835	1272	1648	1968	2236	2458
	5000	BW1	835	1271	1647	1968	2235	2457
		FW1	836	1273	1649	1970	2237	2459

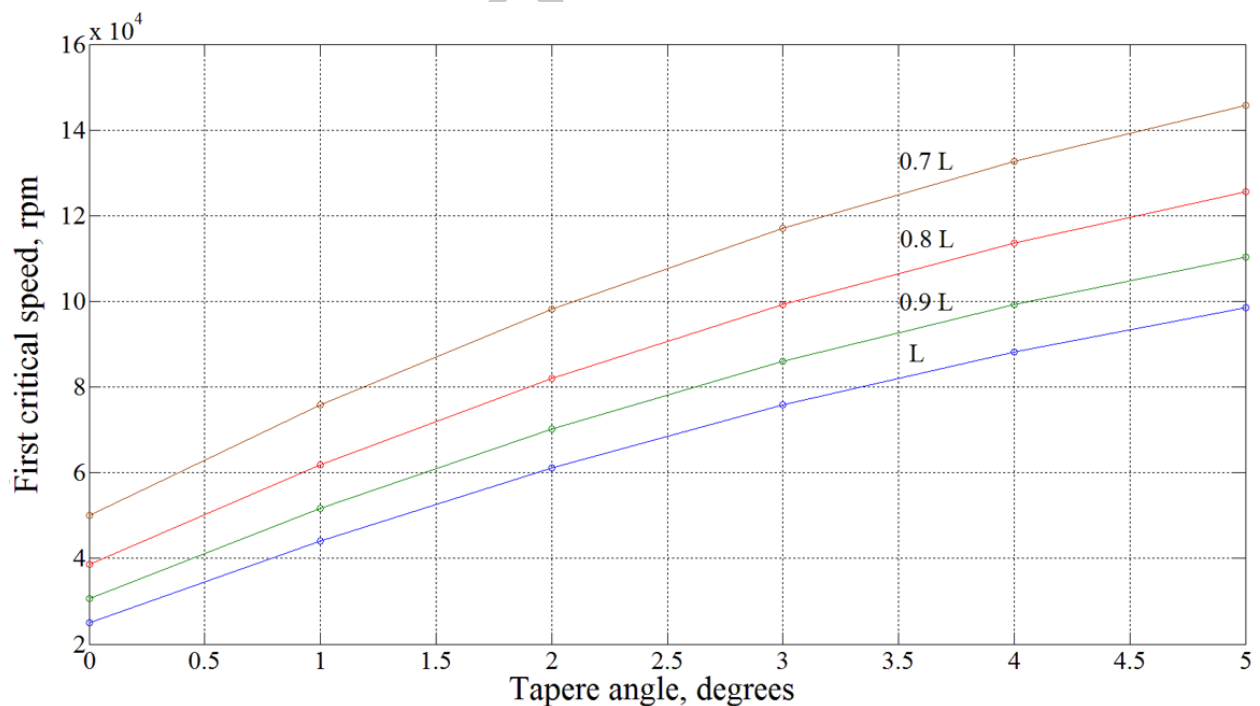


Figure 20 First critical speeds for different lengths determined using hierarchical finite element

### 7.2.2 Effect of shaft diameter on natural frequencies and first critical speed

In this section, the effect of the inner diameter on the natural frequencies and first critical speed is analyzed. The length of the tapered composite shaft  $L$  is fixed at 0.5 m and the configuration of the tapered composite shaft and the stiffness of the bearing are the same as in section 7.2.1. To see its influence on the natural frequencies and first critical speed of the rotating tapered composite shaft, the inner diameter  $d_i$  at the free end is 1 cm and it is varied from  $d_i$  to  $0.7d_i$ . The natural frequency results are illustrated in Table 11, and it can be observed that the natural frequency decreases when the inner diameter at the free end decreases.

In addition, the first critical speeds of the tapered composite shaft are represented in Figure 21. These show that reducing the inner diameter at the free end reduces the critical speed. Also, when the taper angle increases, the difference between first critical speeds decreases. For instance, when the taper angle is  $0^\circ$  the first critical speeds of the tapered composite shaft obtained using the hierarchical finite element are 24,952 rpm and 19,427 rpm for inner diameters  $d_i$  and  $0.7 d_i$ , respectively. But, when the taper angle is  $5^\circ$  the first critical speeds become 98,457 rpm and 96,671 rpm for  $d_i$  and  $0.7 d_i$ , respectively. The difference between first critical speed values for  $5^\circ$  is less than the difference for  $0^\circ$ .

Table 11 Natural frequencies in Hz of the tapered composite shaft at 5000 rpm for different diameters obtained using hierarchical finite element.

Diameter, cm	Mode	Taper angle, degrees					
		0°	1°	2°	3°	4°	5°
$d_i = 1$ cm	BW1	415	737	1022	1271	1482	1657
	FW1	416	738	1024	1273	1484	1660
0.9 $d_i$	BW1	385	709	998	1252	1467	1647
	FW1	386	710	1000	1254	1469	1649
0.8 $d_i$	BW1	354	680	974	1232	1452	1636
	FW1	355	681	975	1234	1455	1639
0.7 $d_i$	BW1	323	651	950	1213	1438	1624
	FW1	323	653	951	1210	1440	1629

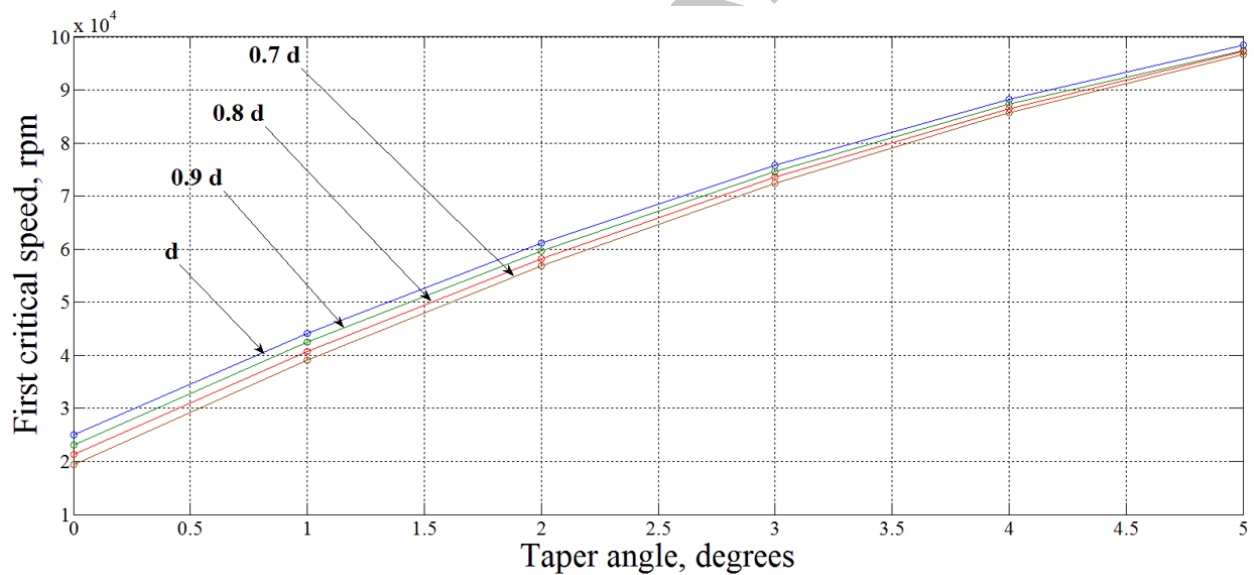


Figure 21 First critical speeds for different diameters obtained using hierarchical finite element

### 7.2.3 Effect of fiber orientation on the natural frequencies and first critical speed

In the following example, the influences of ply orientation angle on natural frequencies and first critical speed of the tapered composite shaft are studied. The configuration and material properties of the tapered composite shaft from section 7.2.1 are considered. The ten layers have the same fiber orientation, and the lamination angles vary from  $0^\circ$  to  $90^\circ$  to investigate their effects on the natural frequencies and the first critical speed.

Table 12 presents the natural frequency of the tapered composite shaft with different lamination angles. According to the results in the tables, the natural frequencies and first critical speed of the tapered composite shaft decrease with increasing fiber orientation angles of the layers and vice versa. Moreover, Figure 22 shows the first critical speeds that were obtained using hierarchical finite element. According to the results in Figure 22, at  $0^\circ$  taper angle, the first critical speeds of the tapered composite shaft are close to each other for fiber orientation angle  $45^\circ \leq \eta \leq 90^\circ$ , for example the first critical speed for  $45^\circ$  and  $90^\circ$  are 14796 rpm and 13934, respectively, and the difference between the two first critical speeds is 5.8 %. However, when the taper angle is  $5^\circ$ , the variation between the first critical speeds for fiber orientation angle  $45^\circ \leq \eta \leq 90^\circ$  is clearly noticeable where the first critical speed for  $45^\circ$  is 70189 rpm and for  $90^\circ$  is 63428 rpm and the difference between the two critical speeds is 9.8 %.

Table 12 Natural frequencies in Hz of the tapered composite shaft at 5000 rpm with different fiber orientation angles obtained using hierarchical finite element

Fiber orientation angle	Mode	Taper angle, degrees					
		0°	1°	2°	3°	4°	5°
0°	BW1	469	810	1078	1281	1431	1542
	FW1	469	811	1079	1282	1432	1543
45°	BW1	244	445	640	831	1016	1192
	FW1	245	446	642	832	1019	1196
60°	BW1	236	432	624	813	999	1179
	FW1	237	433	626	816	1002	1183
90°	BW1	232	420	599	769	928	1073
	FW1	232	421	601	771	930	1076

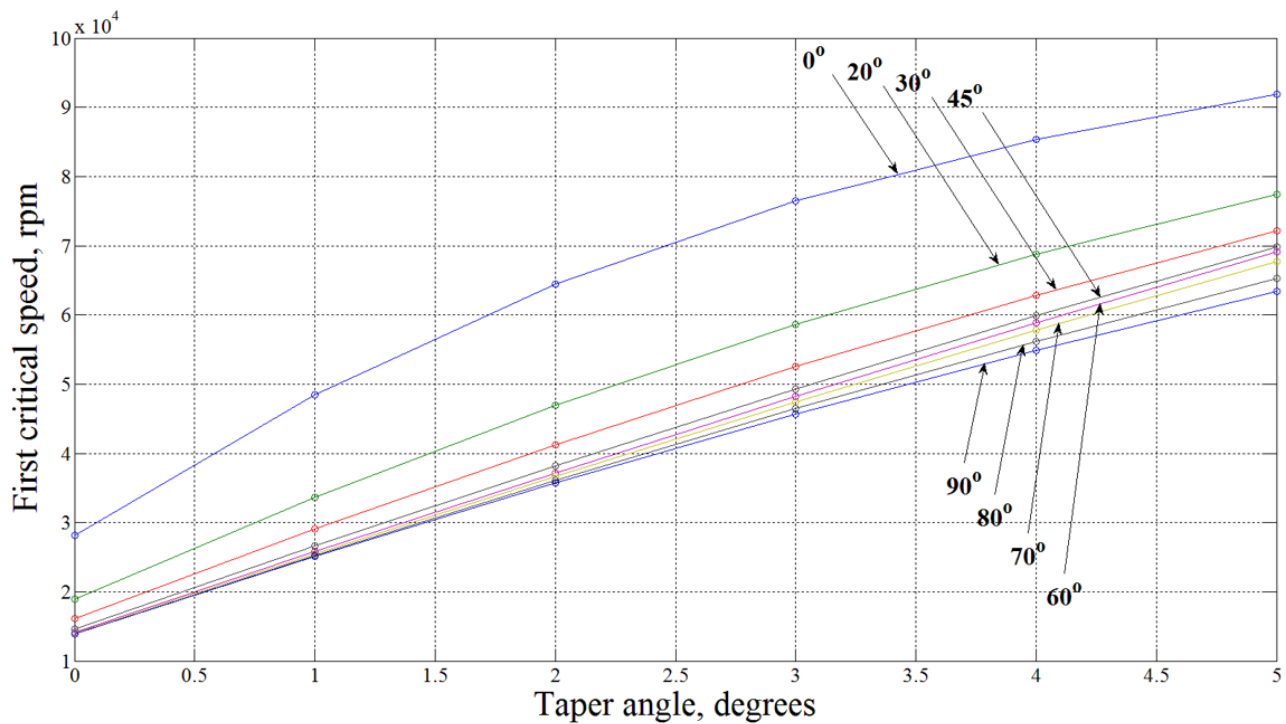


Figure 22 First critical speeds for different fiber orientation angles based on hierarchical finite element

#### 7.2.4 Effect of the stiffness of the bearing on the first critical speed

This section shows how a bearing's stiffness can influence the first critical speed of the tapered composite shaft. This analysis is conducted using the tapered composite shaft from section 7.2.1. The stiffness of the bearing varies from 0.01 MN/m to 10 GN/m. Figure 23 presents the variation of the first critical speed of the tapered composite shaft for various levels of bearing stiffness. The figure shows that, at low bearing stiffness, increasing the taper angle decreases the first critical speed; despite the fact that, at high bearing stiffness, increasing the taper angle increases the first critical speed. In addition, it can be observed from the figure that at a small taper angle the required stiffness for the bearing to be considered as simply supported condition, which is the condition that increasing the stiffness of the bearing does not affect the first critical speed and the natural frequencies any more, is lower than the stiffness required for the bearing at large taper angle.

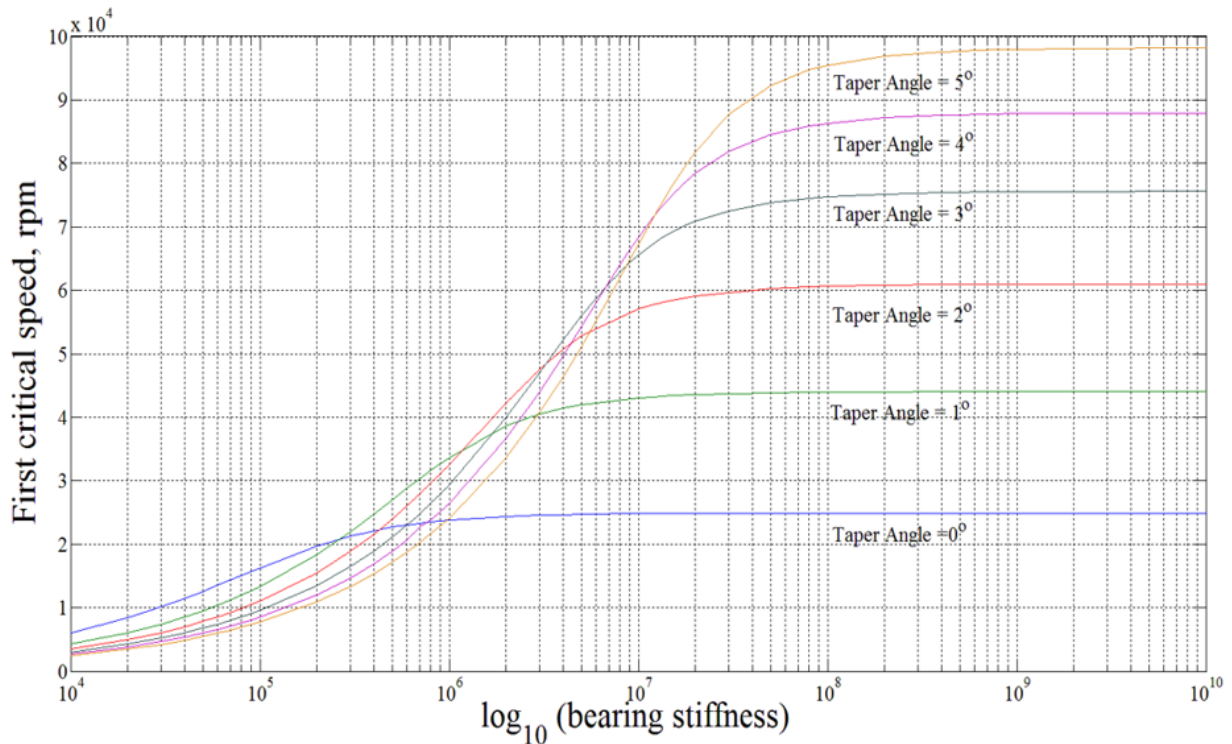


Figure 23 First critical speed for different bearing stiffness values determined using hierarchical finite element.

### 7.2.5 Effect of axial load on natural frequencies and first critical speed

To study the consequence, on the natural frequencies and first critical speed, of applying axial load, the tapered composite shaft in section 7.2.1 is considered. The tensile and compressive loads are applied at the free end of the tapered composite shaft, and the compressive loads are less than the buckling loads. The results of the natural frequencies and first critical speed of applying the tensile and compressive loads on the tapered composite shaft are illustrated in Table 13, Table 14 and Figure 24 – Figure 26. The natural frequencies and critical speeds are obtained using the hierarchical finite element.

According to the results in the tables and figures, the tensile load increases and the compressive load decreases the natural frequency and critical speed. This is because the tensile load increases the stiffness of the tapered composite shaft, while the compressive load decreases it. In addition, increasing the taper angle increases the natural frequency and the first critical speed for both the tensile and compressive loads.

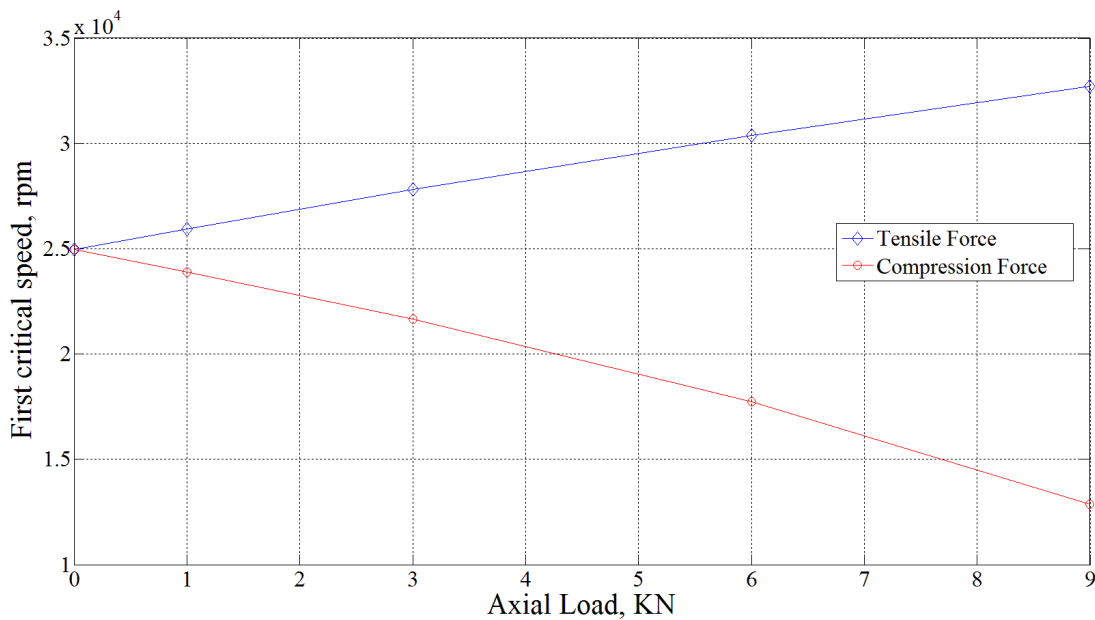


Figure 24 First critical speed of the tapered composite shaft with taper angle of  $0^\circ$  for different axial loads obtained using hierarchical finite element

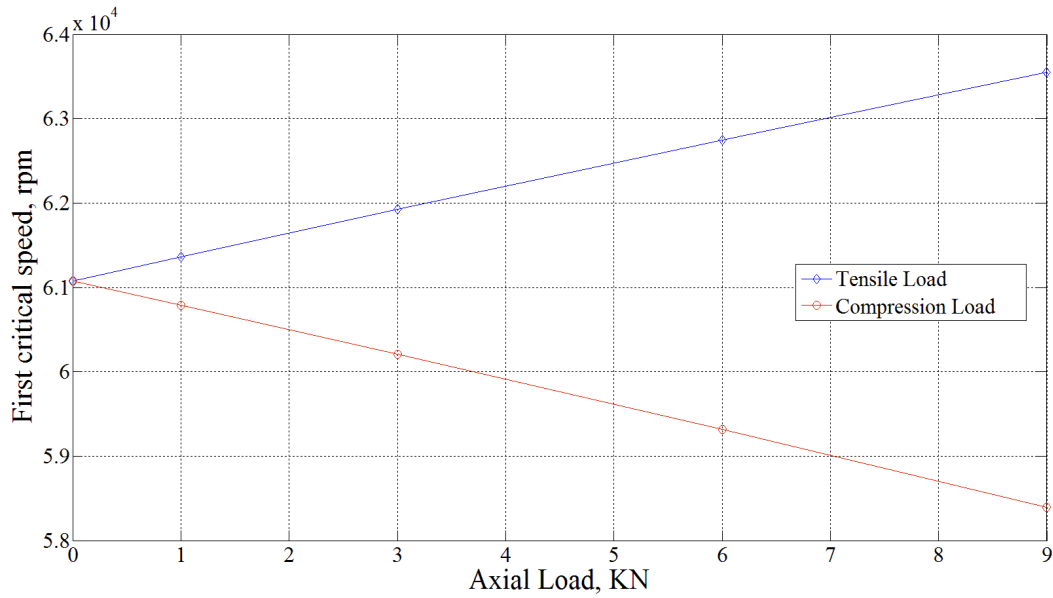


Figure 25 First critical speed of the tapered composite shaft with taper angle of 2° for different axial loads obtained using hierarchical finite element

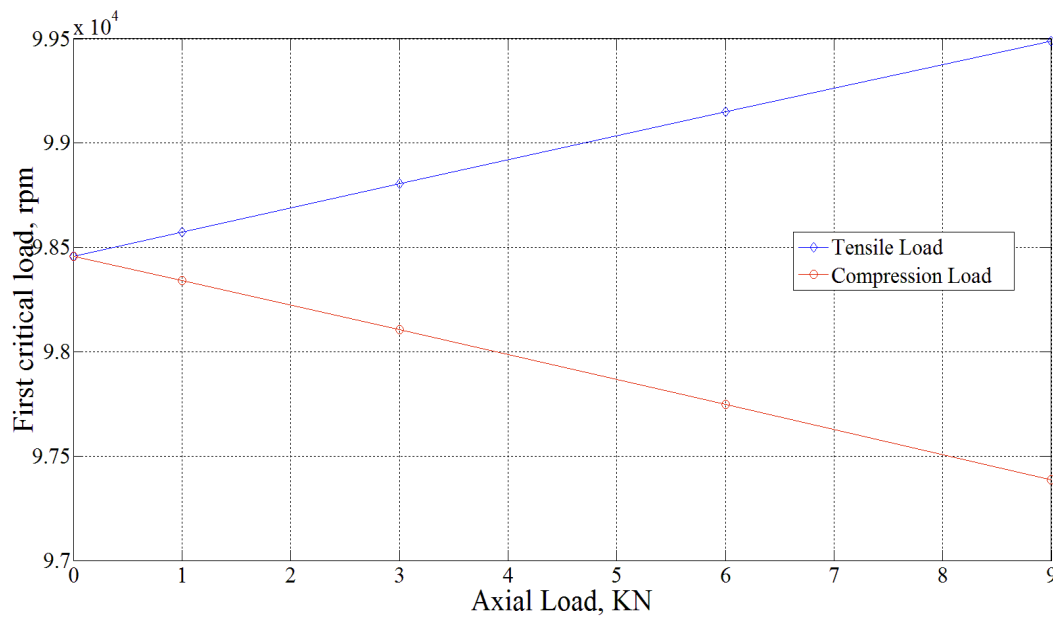


Figure 26 First critical speed of the tapered composite shaft with taper angle of 5° for different axial loads obtained using hierarchical finite element

Table 13 Natural frequencies in Hz of the tapered composite shaft at 5000 rpm with different tensile loads using the hierarchical finite element

Tensile Load (KN)	Mode	Taper angle, degrees					
		0°	1°	2°	3°	4°	5°
1	BW1	433	744	1027	1274	1484	1659
	FW1	434	746	1029	1276	1486	1662
3	BW1	463	759	1037	1281	1489	1664
	FW1	464	760	1038	1283	1491	1665
9	BW1	545	802	1064	1301	1504	1675
	FW1	546	803	1066	1303	1507	1677

Table 14 Natural frequencies in Hz of the tapered composite shaft at 5000 rpm with different compressive loads using hierarchical finite element

Compressive Load (KN)	Mode	Taper angle, degrees					
		0°	1°	2°	3°	4°	5°
1	BW1	398	729	1018	1268	1479	1655
	FW1	398	731	1019	1270	1481	1658
3	BW1	361	713	1008	1261	1474	1651
	FW1	362	715	1006	1263	1477	1654
9	BW1	214	662	977	1240	1459	1639
	FW1	214	663	979	1242	1461	1641

### 7.3 Hybrid tapered composite shaft-disk system

A hybrid composite shaft-disk system with shaft sections of different geometry is considered and studied. The hybrid system consists of three different composite shaft sections and a disk, and the shaft is supported on two bearings. The first shaft section is cylindrical in shape and is of uniform diameter along its length. At one end it is supported on a bearing while at the other end it is connected to a tapered shaft section which is the second shaft section. The largest-diameter end of the tapered shaft section is connected to the first shaft section while the smallest-diameter end is connected to the third shaft section that has a uniform diameter along its length. The second bearing is positioned at the center of the third section, and the disk is located at the free end of the third shaft section. The hybrid composite shaft-disk system is shown in Figure 27. Such a hybrid shaft-disk system would be required in practice to support the shaft properly in bearings that are cylindrical and of uniform size. The dimensions and configuration of the hybrid shaft-disk system are presented in Table 15. The hybrid shaft is made of a graphite-polymer composite material the mechanical properties of which are given in Table 1.

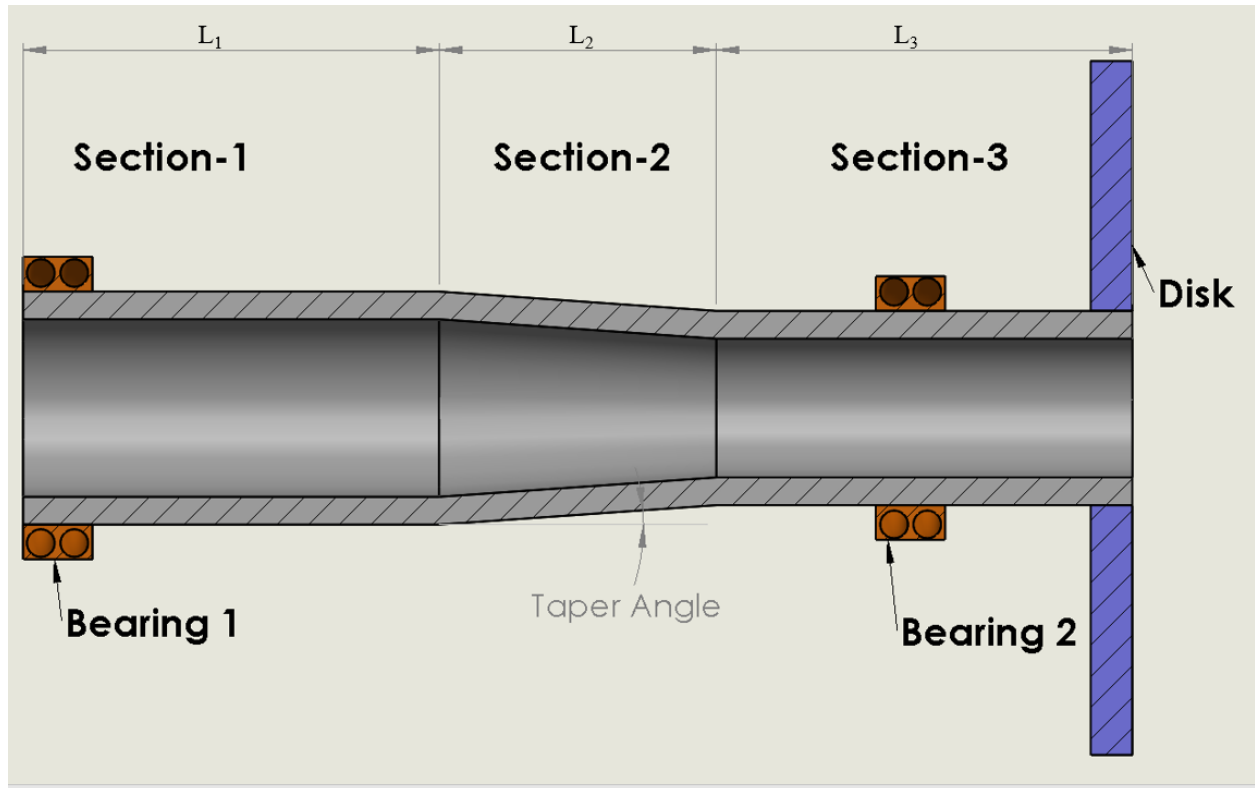


Figure 27 Hybrid composite shaft-disk system

Table 15 Dimensions and configuration of hybrid composite shaft-disk system

<b>Composite Shaft</b>	
Lay-up configuration	[90,45, -45, 06, 90]
Outer diameter (3 <sup>rd</sup> section)	0.04 m
Inner diameter (3 <sup>rd</sup> section)	0.03 m
Taper angle (2 <sup>nd</sup> section)	2°
Wall thickness (All sections)	0.005
Shear correction factor $k_s$	0.525
<b>Disk</b>	
Outer Diameter	0.2 m
Inner Diameter	0.04 m
Thickness	0.02 m
Density	7810 Kg/m <sup>3</sup>
<b>Bearing</b>	
$K_{xx} = K_{yy}$	10 MN/m
$C_{xx} = C_{yy}$	500 N.s/m

For the cases of varying  $L_2/L_1$  and  $L_2/L_3$  length ratio values, the smallest mean diameter of the tapered section does not change with increasing the ratio value because it is connected to the third section which has a fixed mean diameter value, while the largest mean diameter of the shaft changes according to the change in the ratio value. Moreover, since the largest-diameter end of the tapered section is connected to the first section of the hybrid shaft, the inner and outer diameters of the first and second shaft sections remain the same. Figure 28 illustrates the diameter change corresponding to the change in the length ratio value.

The hybrid composite shaft is divided into 12 elements in such a way that each shaft section consists of 4 elements. The length of the element remains the same within each shaft section, but it is of different value from one shaft section to another section depending on the length of the shaft section.

Natural frequencies corresponding to different rotational speeds for the system with hybrid shaft of different length ratio values are presented in Tables 16 - 18. Also, the first critical speeds for the three cases of hybrid shaft-disk system with different length ratio values are listed in Table 19. For the cases with varying  $L_2/L_1$ ,  $L_2/L_3$ , and  $L_1/L_3$  ratio values, the natural frequencies and first critical speed show a decreasing trend with increasing ratio value. In fact, increasing the ratio value leads to the increase in the total hybrid shaft length. It is noted here that the inner and outer diameter values of the third shaft section were fixed for all the ratio values of the three cases.

It is observed from Figure 28 that, as the  $L_2/L_1$  ratio value does increase, the diameters of the first section and the total length of the hybrid composite shaft do increase as well. Although increasing the diameters result in adding more volume of the composite material to the shaft which consequently increase both the stiffness and mass of the shaft, the natural frequencies and critical speeds decrease as the  $L_2/L_1$  ratio increases, due to the combined effects of stiffness and mass increase and their distributions along the longitudinal axis of the shaft.

Table 16 Natural frequencies in Hz for different rotational speeds ( $L_1 = 0.5$  m,  $L_3 = 0.3$  m)

Rotational speed (rpm)	Mode	$L_2/L_1$			
		0.2	0.4	0.6	0.8
0	BW1	74.20	73.10	71.80	70.60
	FW1	74.20	73.10	71.80	70.60
5000	BW1	71.47	70.34	69.11	67.88
	FW1	76.80	75.75	74.57	73.38
10000	BW1	68.74	67.58	66.32	65.09
	FW1	79.35	78.35	77.21	76.04

Table 17 Natural frequencies in Hz for different rotational speeds ( $L_1 = 0.5$  m,  $L_3 = 0.3$  m)

Rotational speed (rpm)	Mode	$L_2/L_3$			
		0.2	0.4	0.6	0.8
0	BW1	74.50	74.00	73.30	72.50
	FW1	74.50	74.00	73.30	72.50
5000	BW1	71.84	71.27	70.58	69.85
	FW1	77.12	76.61	75.98	75.29
10000	BW1	69.12	68.52	67.82	67.08
	FW1	79.65	79.17	78.56	77.90

Table 18 Natural frequencies in Hz for different rotational speeds ( $L_2 = 0.1$  m,  $L_3 = 0.3$  m)

Rotational speed (rpm)	Mode	$L_1/L_3$			
		0.2	0.4	0.6	0.8
0	BW1	200	176.35	153.47	132.88
	FW1	200	176.35	153.47	132.88
5000	BW1	197.51	172.64	149.22	128.59
	FW1	202.34	179.55	157.26	136.82
1000	BW1	194.35	168.36	144.51	123.99
	FW1	204.20	182.31	160.63	140.42

Table 19 First critical speed for the three cases

Ratio	Critical speed (RPM)			
	0.2	0.4	0.6	0.8
$L_2/L_1$	4310	4250	4174	4103
$L_2/L_3$	4331	4298	4259	4217
$L_1/L_3$	11593	10096	8744	7575

$$L_2/L_1 = 0.2 ;$$

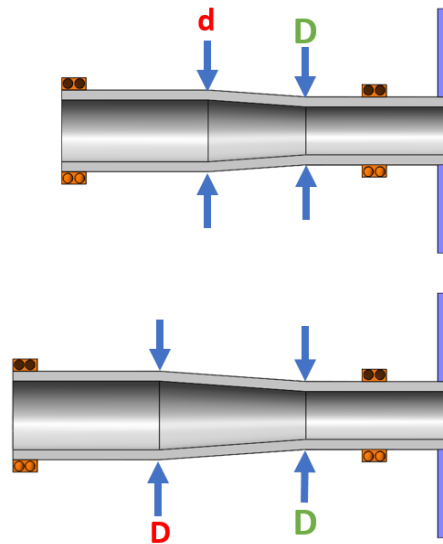
$$(L_1 = 0.5 \text{ m} , L_2 = 0.1 \text{ m} , L_3 = 0.3 \text{ m} )$$

$$D > d$$

D is a Fixed Diameter

$$L_2/L_1 = 0.4 ;$$

$$(L_1 = 0.5 \text{ m} , L_2 = 0.2 \text{ m} , L_3 = 0.3 \text{ m} )$$

Figure 28 The hybrid composite shaft-disk system configuration with different  $L_2/L_1$  ratio values

## 8 Conclusion

In this paper new finite element model have been developed for rotordynamic analysis of the tapered composite shaft. The model developed using the hierarchical finite element formulation. The hierarchical finite element model is based on Timoshenko beam theory, and the effects of rotary inertia, transverse shear deformation, gyroscopic force, axial load, coupling due to the lamination of composite layers, and taper angle are incorporated in the finite element model of the tapered composite shaft. In addition, hierarchical terms are represented in trigonometric function while the polynomial shape function are used to describe the element's nodal degrees of freedom.

To validate the hierarchical finite element model, Rayleigh - Ritz method is used to obtain an approximate solution for simply supported tapered composite shaft. In section 6, a numerical example is given, and it is found that the bending natural frequencies and first critical speeds, for different taper angles of the tapered composite shaft, determined using Rayleigh-Ritz method are in agreement with those obtained using the hierarchical finite element model.

The tapered composite shaft means that the inner and outer diameters of one end are constant while the inner and outer diameters of the other end increase with increasing the taper angle. Consequently, it is found that increasing the taper angle increases the bending natural frequencies and first critical speed of the tapered composite shaft. However, it is seen from the numerical results of Case A in section 7 that this direct relationship between the first critical speed and the taper angle does not sustain because the first critical speed reaches its maximum value at  $10^\circ$  and then starts to drop off with increasing the taper angle.

In section 7, extensive parametric study of the rotordynamic response of tapered composite shaft is presented, and the effects of stacking sequence, fiber orientation angles, taper angle, axial load, bearing stiffness, the inner diameter, and the length of the tapered composite shaft are studied. The important points that can be said about the results in section 7 are the following:

- ✓ Stacking the layers that have high stiffness near the outer surface of the shaft increases the natural frequencies and first critical speed; because the layers near the outer surface have higher volume and circumference than those near the inner surface of the shaft.
- ✓ Increasing the taper angle when using low stiffness bearing decreases the first critical speed; whereas, increasing the taper angle when using high stiffness bearing increases the first critical speed.
- ✓ The natural frequencies and first critical speed of the tapered composite shaft increase with applying tensile load and decrease with applying compressive load along the axial coordinate of the tapered composite shaft.
- ✓ Decreasing the length of the tapered composite shaft and increasing the diameter increase the natural frequencies and the first critical speed and vice versa.

## References

1. Zinberg, H. and Symonds, M.F., "The Development of an Advanced Composite Tail Rotor Driveshaft," The 26th Annual Forum of the American helicopter Society, Washington, DC, June 1970.
2. Chang, M.-Y. Chen, J.-K. and Chang, C.-Y. , "A simple spinning laminated composite shaft model". *International Journal of Solids and Structures*, Vol.41, pp.637–662, 2004.
3. Chang, M.-Y. Huang, J. H. and Chang, C.-Y. , "Vibration analysis of rotating composite shafts containing randomly oriented reinforcements," *Composite structures*, Vol.63, pp.21–32, 2004.
4. Boukhalfa, A. and Hadjoui, A., "Free vibration analysis of a rotating composite shaft using the p-version of the finite element method," *International Journal of Rotating Machinery*, 2008, pp. 10. Article ID 752062.
5. Al Muslmani, M. and Ganesan, R., "Rotor-Dynamics of Stepped Composite Shaft - Disk Systems Based on a Conventional Composite Finite Element," *American Society for Composites 27th Annual Technical Conference*, Arlington, Texas, 2012.
6. Qatu, M. S. and Iqbal, J., "Transverse vibration of a two-segment cross-ply composite shafts with a lumped mass," *Composite Structures*, Vol.92, pp. 1126-1131, 2010
7. Chen, L. and Peng, W., "Dynamic stability of rotating composite shaft under periodical axial compressive loads," *Journal of Sound and Vibration*, Vol.212 (2), pp. 215–230,1998.
8. Na, S., Yoon, H., and Librescu, L., "Effect of taper ratio on vibration and stability of a composite thin-walled spinning shaft," *Thin-Walled Structures*, Vol.44, pp.362–371, 2006.
9. Meirovitch, L. and Baruh, H., "On the inclusion principle for the hierarchical finite element method," *International Journal for Numerical Methods in Engineering*,19:281–91, 1983.
10. ZHU, D., "Development of hierarchical finite element methods at BIAA," *Proceedings of the International Conference on Computational Mechanics*, Tokyo I, 123–128,1986
11. Houmat, A., "A sector Fourier p-element applied to free vibration analysis of sectorial plates," *journal of sound and vibration.*, 243(2), 269-282, 2001
12. WEST, L., BARDELL, N., DUNSDON, J., and LOASBY, P., "Some limitations associated with the use of K-orthogonal polynomials in hierarchical versions of the finite element method," *the Sixth International Conference on Recent Advances in Structural Dynamics*, Southampton, 1997.

13. M. Friswell, J. Penny, S. Garvey, and A. Lees, Dynamics of Rotating Machines, First edition, Cambridge University Press, 2010.
14. T. C. Gmiir and J.D. Rodrigues, Shaft finite elements for rotor dynamics analysis. ASME Vibration Acoustic. 113, 482-493 (1991).
15. W. Kim, A. Argento, and R. A. Scott, Free vibration of a rotating tapered composite Timoshenko shaft, Journal of Sound and Vibration, vol. 226, no. 1, pp. 125–147, 1999.

## Appendix A

$$[M_{11}] = L \int_0^1 m(\xi) [N_v]^T [N_v] d\xi \quad (\text{A.1})$$

$$[M_{22}] = L \int_0^1 m(\xi) [N_w]^T [N_w] d\xi \quad (\text{A.2})$$

$$[M_{33}] = L \int_0^1 m(\xi) [N_{\beta_y}]^T [N_{\beta_y}] d\xi \quad (\text{A.3})$$

$$[M_{44}] = L \int_0^1 m(\xi) [N_{\beta_z}]^T [N_{\beta_z}] d\xi \quad (\text{A.4})$$

$$[G_{34}] = -L\Omega \int_0^1 I_p(\xi) [N_{\beta_y}]^T [N_{\beta_y}] d\xi \quad (\text{A.5})$$

$$[G_{43}] = L\Omega \int_0^1 I_p(\xi) [N_{\beta_z}]^T [N_{\beta_z}] d\xi \quad (\text{A.6})$$

$$[K_{11}] = \frac{1}{L} \int_0^1 k_s (\bar{A}_{55}(\xi) + \bar{A}_{66}(\xi)) [N_v']^T [N_v'] d\xi \quad (\text{A.7})$$

$$[K_{13}] = -\frac{1}{2L} \int_0^1 k_s \bar{B}_{16}(\xi) [N'_v]^T [N'_{\beta_y}] d\xi \quad (\text{A.8})$$

$$[K_{14}] = \int_0^1 \left[ -\frac{1}{L} k_s \bar{B}_{15}(\xi) [N'_v]^T [N'_{\beta_z}] - k_s (\bar{A}_{55}(\xi) + \bar{A}_{66}(\xi)) [N'_v]^T [N'_{\beta_z}] \right] d\xi \quad (\text{A.9})$$

$$[K_{22}] = \frac{1}{L} \int_0^1 k_s (\bar{A}_{55}(\xi) + \bar{A}_{66}(\xi)) [N'_w]^T [N'_w] d\xi \quad (\text{A.10})$$

$$[K_{23}] = \int_0^1 \left[ \frac{1}{L} k_s \bar{B}_{15}(\xi) [N'_w]^T [N'_{\beta_y}] + k_s (\bar{A}_{55}(\xi) + \bar{A}_{66}(\xi)) [N'_w]^T [N'_{\beta_y}] \right] d\xi \quad (\text{A.11})$$

$$[K_{24}] = -\frac{1}{2L} \int_0^1 k_s \bar{B}_{16}(\xi) [N'_w]^T [N'_{\beta_z}] d\xi \quad (\text{A.12})$$

$$[K_{31}] = -\frac{1}{2L} \int_0^1 k_s \bar{B}_{16}(\xi) [N'_{\beta_y}]^T [N'_v] d\xi \quad (\text{A.13})$$

$$[K_{32}] = \int_0^1 \left[ \frac{1}{L} k_s \bar{B}_{15}(\xi) [N'_{\beta_y}]^T [N'_w] + k_s (\bar{A}_{55}(\xi) + \bar{A}_{66}(\xi)) [N'_{\beta_y}]^T [N'_v] \right] d\xi \quad (\text{A.14})$$

$$[K_{33}] = \int_0^1 \left[ \frac{1}{L} \bar{D}_{11}(\xi) [N'_{\beta_y}]^T [N'_{\beta_y}] + k_s \bar{B}_{15}(\xi) ([N'_{\beta_y}]^T [N'_{\beta_y}] + [N'_{\beta_y}]^T [N'_{\beta_y}]) + k_s l + \bar{A}_{66}(\xi) [N'_{\beta_y}] [N'_{\beta_y}] \right] d\xi \quad (\text{A.15})$$

$$[K_{34}] = \int_0^1 \left[ \frac{1}{2} k_s \bar{B}_{16}(\xi) [N'_{\beta_y}]^T [N'_{\beta_z}] - \frac{1}{2} k_s \bar{B}_{16}(\xi) [N'_{\beta_y}]^T [N'_{\beta_z}] \right] d\xi \quad (\text{A.16})$$

$$[K_{41}] = \int_0^1 \left[ -\frac{1}{L} k_s \bar{B}_{15}(\xi) [N'_{\beta_z}]^T [N'_v] - k_s (\bar{A}_{55}(\xi) + \bar{A}_{66}(\xi)) [N'_{\beta_z}]^T [N'_v] \right] d\xi \quad (\text{A.17})$$

$$[K_{42}] = -\frac{1}{2L} \int_0^1 [k_s \bar{B}_{16}(\xi) [N'_{\beta_z}]^T [N'_w]] d\xi \quad (\text{A.18})$$

$$[K_{43}] = \int_0^1 \left[ \frac{1}{2} k_s \bar{B}_{16}(\xi) [N_{\beta_z}]^T [N'_{\beta_y}] - \frac{1}{2} k_s \bar{B}_{16}(\xi) [N'_{\beta_z}]^T [N_{\beta_y}] \right] d\xi \quad (\text{A.19})$$

[K<sub>44</sub>]

$$= \int_0^1 \left[ \frac{1}{L} \bar{D}_{11}(\xi) [N'_{\beta_z}]^T [N'_{\beta_z}] + k_s \bar{B}_{15}(\xi) \left( [N'_{\beta_z}]^T [N_{\beta_z}] + [N_{\beta_z}]^T [N'_{\beta_z}] \right) + k_s L \right. \\ \left. + \bar{A}_{66}(\xi) [N_{\beta_z}] [N_{\beta_z}] \right] d\xi \quad (\text{A.20})$$

$$[K_{pv}] = \int_0^1 P [N'_v]^T [N'_v] d\xi \quad (\text{A.21})$$

$$[K_{pw}] = \int_0^1 P [N'_w]^T [N'_w] d\xi \quad (\text{A.22})$$

## Appendix B

$$[H] = [H_1 \ H_2 \ \dots \ H_n]_{1 \times n} = \left[ \sin \frac{1\pi x}{L} \ \sin \frac{2\pi x}{L} \ \dots \ \sin \frac{n\pi x}{L} \right]_{1 \times n} \quad (\text{B.1})$$

$$[F] = [F_1 \ F_2 \ \dots \ F_n]_{1 \times n} = \left[ \cos \frac{1\pi x}{L} \ \cos \frac{2\pi x}{L} \ \dots \ \cos \frac{n\pi x}{L} \right]_{1 \times n} \quad (\text{B.2})$$

$$[M_V]_{n \times n} = \int_0^L m(x) [H]^T [H] dx \quad (\text{B.3})$$

$$[M_W]_{n \times n} = \int_0^L m(x) [H]^T [H] dx \quad (\text{B.4})$$

$$[M_{B_y}]_{n \times n} = \int_0^L m(x) [F]^T [F] dx \quad (\text{B.5})$$

$$[M_{B_z}]_{n \times n} = \int_0^L m(x) [F]^T [F] dx \quad (\text{B.6})$$

$$[G_{B_z}]_{n \times n} = -\Omega \int_0^L I_p(x) [F]^T [F] dx \quad (\text{B.7})$$

$$[G_{B_y}]_{n \times n} = \Omega \int_0^L I_p(x) [F]^T [F] dx \quad (\text{B.8})$$

$$[K_{V1}]_{n \times n} = \int_0^L k_s (\bar{A}_{55}(x) + \bar{A}_{66}(x)) [H']^T [H'] dx \quad (\text{B.9})$$

$$[K_{V3}]_{n \times n} = -\frac{1}{2} \int_0^L k_s \bar{B}_{16}(x) [H']^T [F'] dx \quad (\text{B.10})$$

$$[K_{V4}]_{n \times n} = \int_0^L \left[ -k_s \bar{B}_{15}(x) [H']^T [F'] - k_s (\bar{A}_{55}(x) + \bar{A}_{66}(x)) [H']^T [F'] \right] dx \quad (\text{B.11})$$

$$[K_{W2}]_{n \times n} = \int_0^L k_s (\bar{A}_{55}(x) + \bar{A}_{66}(x)) [H']^T [H'] dx \quad (\text{B.12})$$

$$[K_{W3}]_{n \times n} = \int_0^L [k_s \bar{B}_{16}(x) [H']^T [F'] + k_s (\bar{A}_{55}(x) + \bar{A}_{66}(x)) [H']^T [F']] dx \quad (\text{B.31})$$

$$[K_{W4}]_{n \times n} = -\frac{1}{2} \int_0^L [k_s \bar{B}_{16}(x) [H']^T [F']] dx \quad (\text{B.41})$$

$$[K_{By1}]_{n \times n} = -\frac{1}{2} \int_0^L [k_s \bar{B}_{16}(x) [F']^T [H']] dx \quad (\text{B.51})$$

$$[K_{By2}]_{n \times n} = \int_0^L [k_s \bar{B}_{15}(x) [F']^T [H'] + k_s (\bar{A}_{55}(x) + \bar{A}_{66}(x)) [F']^T [H']] dx \quad (\text{B.61})$$

$$[K_{By3}]_{n \times n} = \int_0^L [ \bar{D}_{11}(x) [F']^T [F'] + k_s \bar{B}_{15}(x) ([F']^T [F] + [F]^T [F']) + k_s (\bar{A}_{55}(x) + \bar{A}_{66}(x)) ] dx \quad (\text{B.71})$$

$$[K_{By4}]_{n \times n} = \int_0^L \left[ \frac{1}{2} k_s \bar{B}_{16}(x) [F']^T [F] - \frac{1}{2} k_s \bar{B}_{16}(x) [F]^T [F'] \right] dx \quad (\text{B.18})$$

$$[K_{Bz1}]_{n \times n} = \int_0^L [ -k_s \bar{B}_{15}(x) [F']^T [H'] - k_s (\bar{A}_{55}(x) + \bar{A}_{66}(\xi)) [F]^T [H'] ] dx \quad (\text{B.91})$$

$$[K_{Bz2}]_{n \times n} = -\frac{1}{2} \int_0^L [k_s \bar{B}_{16}(x) [F']^T [H']] dx \quad (\text{B.20})$$

$$[K_{Bz3}]_{n \times n} = \frac{1}{2} \int_0^L [k_s \bar{B}_{16}(x) [F]^T [H'] - k_s \bar{B}_{16}(x) [F']^T [H]] dx \quad (\text{B.21})$$

$$[K_{Bz4}]_{n \times n} = \int_0^L [ \bar{D}_{11}(x) [F']^T [F'] + k_s \bar{B}_{15}(x) ([F']^T [F] + [F]^T [F']) + k_s (\bar{A}_{55}(x) + \bar{A}_{66}(x)) ] dx \quad (\text{B.22})$$

ACCEPTED MANUSCRIPT